Chemical Science

Accepted Manuscript

This article can be cited before page numbers have been issued, to do this please use: S. Li, J. Li, X. Wang, M. Li, T. Lu, H. Li, Y. Tang and G. Fu, *Chem. Sci.*, 2026, DOI: 10.1039/D6SC03404G.

ROYAL SOCIETY OF CHEMISTRY

rsc.li/chemical-science

View Article Online
DOI: 10.1039/D6SC03404G

Localized hetero-ion modulation engineering over nickel-based catalyst for electrochemical urea oxidation

Shucheng Li,[†,a] Jing Li,[†,a] Xuan Wang,*[a] Meng Li,[a] Tingyu Lu,[b] Hao Li,[b] Yawen Tang,*[a] Gengtao Fu*[a]

[a] Jiangsu Key Laboratory of New Power Batteries, Jiangsu Collaborative Innovation Center of Biomedical Functional Materials, Jiangsu Key Laboratory of Micro Nano Sensing and Separation Science for Analytical Chemistry, School of Chemistry and Materials Science, Nanjing Normal University, Nanjing 210023, China.
E-mail: wangxuan@njnu.edu.cn; tangyawen@njnu.edu.cn; gengtaofu@njnu.edu.cn

[b] Advanced Institute for Materials Research (WPI-AIMR), Tohoku University, Sendai 980-8577, Japan.

[†]These authors contributed equally to this work.

Abstract: Electrochemical urea oxidation reaction (UOR) offers the effective alternative for oxygen evolution reaction (OER) in electrochemical production of hydrogen source, yet the nickel (Ni)-based catalysts show the inferior reaction kinetics. To address the performance limitations, localized hetero-ion modulation for intrinsic properties of Ni-based catalysts has evolved to meet the practical expectations. The modulation over local coordination environment by incorporated hetero-ion is imperative for enhancing the intrinsic catalytic activity and efficiency of nickel-based catalysts. Illuminated by the profound influence, a systematic comprehension of localized hetero-ion modulation over UOR is instantly supplied in this review to construct the atomic insight for catalytic mechanism and catalyst design within Ni catalyst. Beginning with the introduction of electrochemical reaction pathways for UOR, the physiochemical properties of $Ni(OH)_2$ and universal scaling relations of reaction intermediates are depicted to guide the fundamental understanding of structure-derived electrochemical behavior for UOR. Subsequently, the specific functions of hetero-ion species for enhancement of UOR in Ni catalyst are delved into the closed relation between localized reaction site formats and reaction pathways. In the end, a closed-loop framework with conclusion of this review is delivered over hetero-ion modulation formats to advance the data-driven catalysis investigation

View Article Online
DOI: 10.1039/D6SC03404G

of electrochemical UOR within Ni catalyst. We believe that this review will attract pronounced attention for advancement of electrochemical UOR.

Keywords: Urea oxidation; Nickel catalyst; Localized hetero-ion modulation; Active unit site; Mechanism insight

1. Introduction

With the global pursuit of ever-increasing consumption of fossil fuels, the detrimental environmental concerns are posing challenges for rapid advancement of sustainable energy resources.[1-6] To overcome the severe environmental crisis, tremendous attempts have been devoted to the novel energy systems including green hydrogen, nitrogen cycle, carbon dioxide cycle, and so forth.[7-11] Notably, electrochemical water splitting is renowned as the flexible system that is able to couple with renewable solar, wind, and tidal power sources.[12-18] However, originating from the four-electron transfer, the sluggish kinetics of anodic oxygen evolution reaction (OER) largely limits the hydrogen production efficiency as the significant bottleneck.[19-21] In contemporary, electrochemical oxidation of various organic molecules has been discovered to replace the energy-burdened water splitting progress, including alcohols, amines, hydrazine, and so forth.[22-26] Among these promising candidates, the electrochemical urea oxidation reaction (UOR) has garnered enhanced attention as an effective solution to this drawback with the small organic molecule oxidation, due to the available feedstock from wastewater and animal metabolism.[27, 28] More importantly, owing to the low thermodynamic equilibrium potential, UOR can remarkably decrease the electrolytic voltage and energy consumption compared with alcohol oxidation. Meanwhile, roughly 80% of the domestic and industrial wastewater containing urea, and UOR achieves simultaneous wastewater denitrification and hydrogen production, alleviating the toxic ammonia influence that contributes to the acid rain, thus facilitating the beneficial cycle in the agricultural ecosystem.[29-31]

In principle, the thermodynamic equilibrium potential of UOR is assigned to be 0.37 V versus reversible hydrogen electrode (vs. RHE), stating the chemical conversion of urea into harmless products such as H_2O, CO_2 and N_2, which is obviously lower than that of driving OER

View Article Online
DOI: 10.1039/D6SC03404G

of 1.23 V (Fig. 1a).[32-36] Therefore, the replace for OER by UOR is able to supply the cost decrease by ~36% in terms of hydrogen production. Furthermore, benefiting from the unique gravimetric hydrogen content (6.7 wt%), urea also acts as the hydrogen carrier that fetches the application in direct urea fuel cells (Fig. 1b).[37-39] With the direct coupling between UOR and hydrogen evolution, the utilization of urea electrolysis further provides the advancing energy conversion framework, benefiting the simultaneous approach of hydrogen production and purification of urea-abundant wastewater. However, the practical application of UOR within these frameworks is still deterred by the sluggish six-electron transfer kinetics, side reactions for the release of pollutants (e.g. NO_2^-, CNO^-), and the detrimentally irreversible phase transformation of nickel oxides under the operando oxidative conditions, thus resulting in the urgent requirement of designing and discovering highly-effective catalysts.[40-42]

With respect to the urea molecule, the molecular connection between carbonyl group (C=O) and amino groups ($–NH_2$) contributes to the polarized property, where the C=O group area mainly acts as the electron-negative accumulation while animo group area behaves as the electron-positive depletion (Fig. 1c). Benefiting from such topological polarization, the specific chemical adsorption of urea molecule by electrostatic interaction discloses the non-identical splitting pathways during the electrochemical oxidation process, depending on the local electrophilic and nucleophilic property of the catalyst surface sites.[43-45] As the most promising non-noble candidates, nickel-based catalysts have emerged for UOR owing to the adjustable active sites and low cost since the initiation by Botte et al in 2009, where the employment of $Ni(OH)_2$ reveals the performance in alkaline condition (Fig. 1d).[46-49] However, limited by the insufficient reaction rate and catalytic degradation under practical application conditions, the intrinsic performance of $Ni(OH)_2$ should still be modulated through external strategies, including incorporation of defects, construction of active phases, and crystallinity evolution, as concluded in several recent reviews and works.[50-57] Despite these focus on the modulation strategies over nickel-based catalysts, the localized hetero-ion modulation provides the atomic precision to target at the effective enhancement of UOR and the straightforward model for understanding the reaction mechanisms based on the active unit site simultaneously. More specifically, the atomic-precision doping of hetero-ion on Ni-based materials can modulate the coordination environment of Ni active sites effectively. Meanwhile, interfacial electron transfer

View Article Online
DOI: 10.1039/D6SC03404G

and orbital hybridization between hetero-ion and Ni sites can also regulate the d-band center and valence state configuration of Ni species, thereby decreasing the adsorption strength of UOR reaction intermediates and significantly boosting the catalytic activity. Therefore, localized hetero-ion modulation exhibits unique advantages in Ni-based materials and exhibits important research significance. However, to approach such chemical insight, a dedicated review is urgently warranted over the exclusive announcement for localized hetero-ion modulation in light of structure-derived catalytic mechanism, which motivates the deep comprehension over rational design of highly-performed UOR candidates.

Herein, in this review, we mainly concentrated on the most advancement of localized modulation from the incorporation of hetero-ions into Ni-based catalysts that forms the unique unit active site for electrochemical UOR. To lead the insightful atomic comprehension over the localized modulation framework, the basic electrochemical mechanism of UOR over Ni-based catalysts is first discussed briefly including physiochemical properties of $Ni(OH)_2$ and universal scaling relations of the free energy of reaction intermediates. Afterwards, the detailed catalyst-driven reactions are then supplied by the strictly entangled discussion over hetero-ion coordination formats, UOR performance, and oxidation pathways, where the hetero-ions witness the evolution from main group, transition-metal species, towards rare-earth kinds. Finally, the conclusion of this review and outlook for future development of data-driven catalysis over UOR based on closed-loop framework is proposed, aiming at the comprehensive advancement of novel and highly-performed nickel-based catalysts. The chemical insights obtained from this review are hopeful to guide the future novel discovery of highly-performed nickel-based catalysts to tackle the fundamental bottlenecks of electrochemical urea splitting.

View Article Online
DOI: 10.1039/D6SC03404G

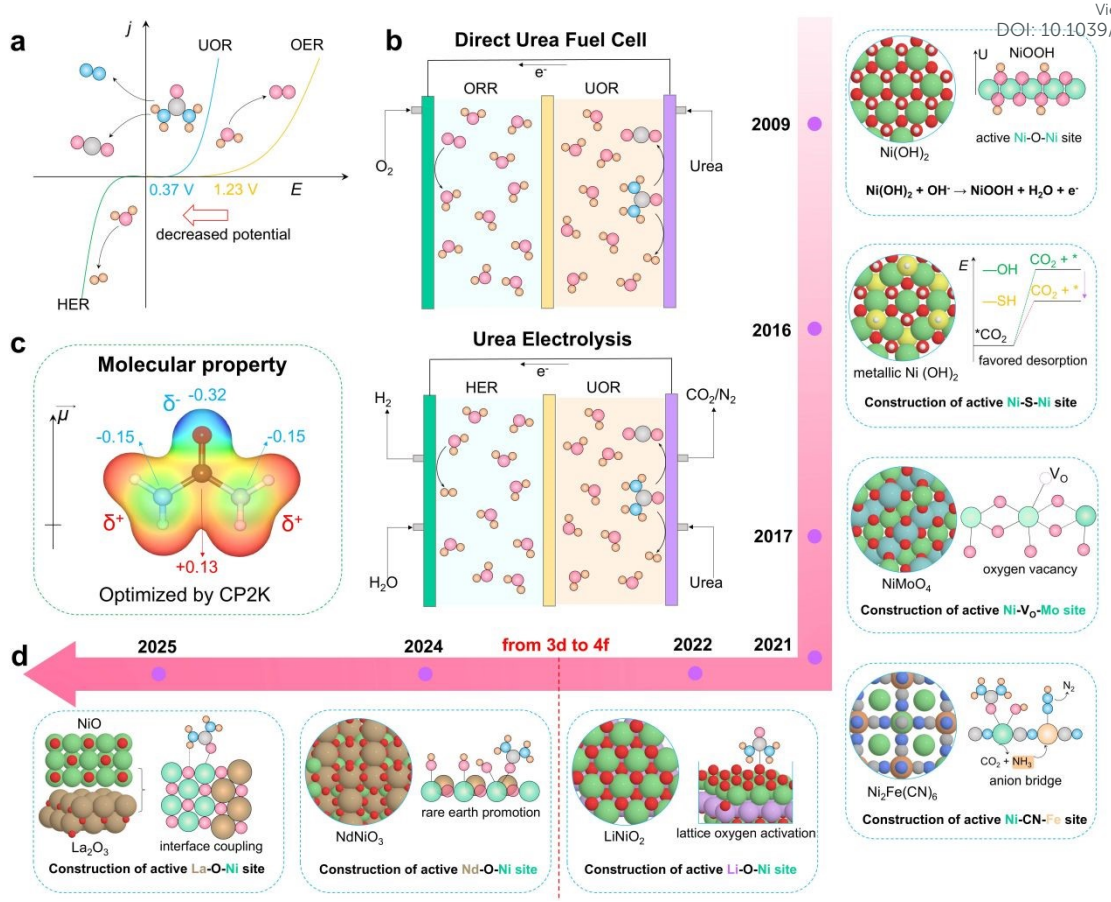

Fig. 1. (a) Qualitative display of the polarization curves for electrochemical urea oxidation, oxygen evolution, and hydrogen evolution; (b) Schematic diagrams for direct urea fuel cell and urea electrolysis systems; (c) Molecular property of urea molecule with electrostatic potential distribution and Mulliken population analysis, optimized by CP2K code under RPBE-D3(BJ)/DZVP-MOLOPT-SR-GTH, where iso-surface value is set to be 0.15 (a.u.);[58-67] (d) Timescale for the progress of localized modulation over Ni catalyst in UOR.

2. Mechanical insight for electrochemical UOR

2.1. Typical reaction pathways

As similar with OER, UOR in aqueous solution occurs at the anode in urea-driven electrochemical systems, which experiences the complex multiple H^+/e^- transfer steps along with specific chemical steps. The typical format of UOR follows $CO(NH_2)_2 + H_2O \rightarrow N_2 + 3H_2 + CO_2$, requiring the thermodynamic potential of 0.37 V that is lower than that of OER.[68, 69] However, due to a greater number of electron transfer with complex chemisorption behavior of various intermediates, the slower reaction kinetics and complicated side reactions still necessitate the determination and discovery of highly-effective pathways for urea splitting,

which is vital for reducing the cost for green hydrogen production and degradation of agricultural pollution to the economic view. Presently, several reaction pathways have been proposed over Ni-based materials for potential-driven splitting of urea through sophisticated physical characterizations and theoretical investigations. The representative mechanisms of UOR are discussed over typical nickel-based (notably the nickel hydroxide) catalysts briefly in this section.

In principle, the UOR should proceed through the chemical adsorption of urea molecule over the active sites of catalysts, where the consecutive release of proton and electron drives the cleavage of C–N and the coupling of N–N bond, till the creation of final products including NH_3, N_2, NO_2^-, NO_3^-, CO_2, CO_3^{2-}, and so forth, depending on the oxidation condition of the Ni-based catalyst surface.[70, 71] Since the UOR appears in the oxidative potential window, the oxidation of Ni-based catalysts is unavoidable. Initially, it is captured by Botte et al that the $Ni(OH)_2$ in basic media can be oxidized into NiOOH, where the chemical transition from Ni^{2+} into Ni^{3+} is noted as the active state.[72] Afterwards, Botte et al also performed the theoretical investigation for the dissociation rate of urea over NiOOH catalysts.[73] It is illustrated that the absence of OH^- can promote the transformation of urea into NH_3 and HNCO with the formation of NH_3 as the rate-limiting step (RDS) of 1.5×10^{-6} s^{-1}, while the presence of hydroxide assigns the creation of NH_3 as the RDS with the rate of 1.4×10^{-26} s^{-1}. The deactivation of UOR performance derived from the surface blockage by $*CO_2$ confirms the catalytic role of OH^- attack for the splitting of urea molecule, paving the initial prototype for the nucleophilic attack mechanism over NiOOH. As shown in Fig. 2a, the nucleophilic OH^- attack for UOR was first proposed over nickel catalyst, where the Ni site mainly experiences the splitting of urea molecule for the first stage.[74] In detail, the urea molecule is first adsorbed at the active Ni site through oxygen coordination, and afterwards, the consecutive OH^- attack towards the C–N bond leads the formation of $*OCONH_2$ and the release of NH_3. At the second stage, the OH^- attack further transforms the NH_3 into $*NH_2$, and the consecutive intermolecular coupling between two adjacent $*NH_2$ species guides the formation of N_2 through various release of H^+/e^- over the active Fe sites via the electrochemical oxidation of $*NH_2$ ($*NH_2NH_2 \rightarrow *NHNH_2 \rightarrow *NNH_2 \rightarrow *NNH \rightarrow N_2$).

View Article Online
DOI: 10.1039/D6SC03404G

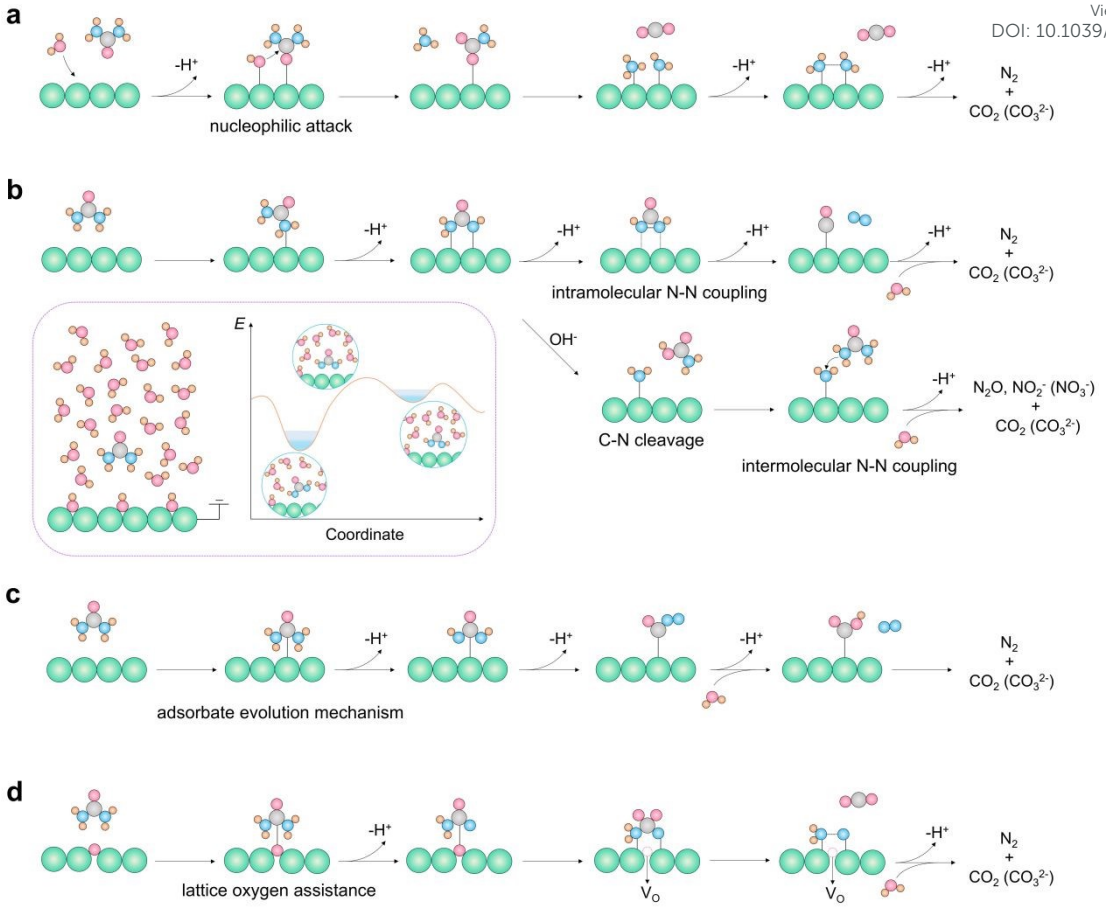

Fig. 2. (a-b) Nucleophilic attack mechanism and intramolecular coupling mechanism. (c-d) Adsorbate evolution mechanism and lattice oxygen assistance mechanism. The green, blue, grey, red, and orange balls represent catalyst surface, nitrogen, carbon, oxygen, and hydrogen atoms, respectively. The inset plot shows the schematic diagram of anodic surface distribution of urea and solvents, where the reaction proceeding is proposed to experience the dynamic surface state change with solvent reorganization and configuration shift of adsorbates that can be projected over the potential energy surface during intramolecular N–N coupling process.

By noting about the splitting process of urea molecule, it witnesses that cleavage of C–N bond takes the central role in terms of the formation of final products such as CO_2 and N_2. However, such cleavage typically involves the reconstruction of $–CONH_2–$ group, including the intramolecular and intermolecular N–N coupling over $Ni(OH)_2$ (Fig. 2b).[75] In terms of the intramolecular N–N coupling mechanism, the urea molecule experiences the adsorption and the consecutive release of H^+/e^- to form the transformation of $*CONHNH_2$ into *CONHNH. The next coupling between two –NH groups within *CONHNH create the product of *CO and N_2, where the adsorbed *CO directs the find product of CO_2 (CO_3^{2-}) in alkaline media under

View Article Online
DOI: 10.1039/D6SC03404G

oxidative condition. Practically, the over-oxidation of NiOOH derived from $Ni(OH)_2$ phase often deviates the innocuous N_2 product into oxidative species such as N_2O and NO_2^- (NO_3^-), which is the intermolecular N–N coupling after the C–N cleavage by OH^- attack with the assistance of additional urea molecules. Specifically, with the nucleophilic attack from OH^- species in alkaline electrolyte, the C–N cleavage of $*CONHNH_2$ forms the $*NH_2$ and intermediate product of NH_2–COOH, where the further attack by OH^- species towards $*NH_2$ is able to release of products such as NO_2^- and NO_3^-. The proceeding of intermolecular N–N coupling after the C–N cleavage can be facilitated by increasing the concentration of urea, which promotes the formation of N_2O. The existence of the competitive intermolecular N–N coupling can be attributed to the high energy barrier when the two N atoms approach each other that contributes to the intermolecular N–N coupling, where the kinetics of C–N cleavage by OH^- attack is more favorable compared with the formation of $*CON_2$.

Additionally, it witnesses that the competitive OER possesses the similar potential window as with UOR to some extent. Thus, the participation of H_2O and the nucleophilic attack by OH^- within the above UOR mechanism may also rationalize the typical pathways as from OER, notably the adsorbate evolution mechanism (AEM) and lattice oxygen mechanism (LOM) over $Ni(OH)_2$. In terms of AEM pathway (Fig. 2c), as similar with the above N–N coupling, the previous steps experience the adsorption of urea molecule, the dehydrogenation for the formation of $*CONH_2NH_2$ intermediate. The key step in AEM pathway lies in the intramolecular N–N coupling of $*CON_2$ after the dehydrogenation of $*CONH_2NH_2$, where the subsequent formation of *COOH from *CO is available to guide the electrooxidation into CO_2. Among these elementary steps, the desorption of $*CO_2$ is assumed to be the most rate-determining step (RDS) that limits the overall UOR process. Distinct from the AEM pathway, LOM pathway is assigned with the expediated kinetics which involves the redox of lattice oxygen as the nucleophilic attack site (Fig. 2d). The activated lattice oxygen site is able to combine with urea molecule that forms the oxygen vacancies during the UOR process, thus completing the whole catalytic loop. After the formation of $*CO_2NNH_2$, the C–N cleavage with dehydrogenation allows for the creation of $*NH_2$ and *N at the catalyst surface with the release of CO_2 as the product. The final coupling between $*NH_2$ and *N leads the formation of N_2 as the product.

View Article Online
DOI: 10.1039/D6SC03404G

Furthermore, distinctive UOR processes can also occur in neutral or acidic media, where the NaCl or HCl act as the solute. However, it should be pointed out that the oxidation of Cl^- is also unavoidable during the electrooxidation progress that creates the side products such as HClO and Cl_2 with oxidative power. The disadvantages for electrolytes beyond alkaline media are comprised of the low Faradaic Efficiency due to the existence of side reactions and the shortened lifespan for Ni-based materials due to the harsh H^+ electrolyte and highly oxidation condition. As a result, few works are concentrated over acidic UOR processes compared with neutral and alkaline media. Undoubtedly, the deep insight into the comprehension of UOR will largely drive the novel guidance and design for efficient transformation systems.

2.2. Electrochemical property of active $Ni(OH)_2$ phase

Nickel hydroxide typically exhibits the prototype of layered structure that are distinctive of common transition-metal-based oxides, where the direct expose of surface –OH sites provides the abundant H^+/e^- transfer kinetics. With the interlayer insertion of water molecules and alkaline metal cations, different bulk phases are available, being comprised of α-$Ni(OH)_2$ and β-$Ni(OH)_2$.[76] When serving as the electrocatalysts, the exposure of $Ni(OH)_2$ towards the harsh conditions including high electrolyte pH and oxidative bias potential undergoes the phase transition into NiOOH and NiO_2 with the depletion of surface H sites (Fig. 3a). The increase of oxidation number of Ni^{2+} into Ni^{3+} in NiOOH and even Ni^{4+} in NiO_2 equips the Ni site with oxidation power that drive the electrochemical oxidation reactions such as OER, alcohol oxidation, and UOR. Notably, under the certain pH and bias potential condition, the water molecule will experience the electrochemical equilibrium with $Ni(OH)_2$ surface through the coverage effect of various intermediates, which further affects the reaction progress. As shown in Fig. 3b, the *ab inito* energy of various *H coverage states over NiOOH surface was used to construct the surface Pourbaix diagram.[77] The horizontal line was taken as the basic reference, denoting the fully deprotonated surface at pH = 14 both for surface and subsurface *H coverage. It should be noted that below U < 0.7 V (vs. SHE), the most state should be fully covered with *H both for surface and subsurface. The further increase of bias potential will promote the deprotonation with decrease surface coverage of *H that drive the deep phase transformation from NiOOH into NiO_2. Concerning the potential window for UOR, the electrochemical stable

phase assigns the transition between $Ni(OH)_2$ and NiOOH, where the Ni^{3+} site with higher oxidation number is promising to act as the active center as is typically different from the competitive OER process.

By noticing about the electrochemical driven phase transition for active $Ni(OH)_2$ phase, the change of coordination environment around Ni is found to modulate the intrinsic electrochemical property. Taking Fe iron as the model, Zhou et al unveiled the dynamic surface state change under oxidative condition in terms of the formation of several metastable NiO_xH_y phases and Fe doping effects.[78] As shown in Fig. 3c, with the incorporation of Fe, the phase equilibrium potentials all decrease compared with the undoped condition under the same pH window. Such phenomenon states that the incorporation of Fe into $Ni(OH)_2$ facilitates the oxidation of Ni^{2+} into higher oxidation state, which is vital to drive the electrochemical oxidation. Notably, the pH window for $Ni(OH)_2$ phase area is extended after the Fe doping, implying the enhanced tolerance for the pH change to promote the phase stability towards harsh electrolyte. In terms of the exfoliated gel-like structure, Fe ions are able to be inserted into the interlayer with more complex coordination with water molecules or layered hydroxyls of NiO_xH_y surface, which is determined by the favorable adsorption catalyst of octahedral Fe^{2+} structure. To further testify the dynamic change of water intercalation with adsorbed Fe species, various configurations of Fe-$(H_2O)_x$ structure were further investigated within ab initio molecular dynamics (AIMD) simulations (Fig. 3d). To understand the Fe-induced dynamic change of local structure, various models are referred including 2UP, 3UP, 2UP-TETRA, 3UP-TETRA, 2IN6, 3IN6, BRIDGE, and TILT models. Among these models, the 2UP and 3UP models are more active that the coordinated H_2O with Fe^{2+} (2UP model) and Fe^{3+} (3UP model) is easier to provide the surface oxygen of NiOOH with released proton to lead the dynamic phase equilibrium. Compared with Fe^{2+}, the coordinated H_2O with Fe^{3+} center favors the splitting to attract the more OH^- species, implying the enhanced electrified field induced by the highly positive charge of Fe^{3+}. With the increased coordinated O around Fe^{3+} such as in BRIDGE model, high oxidation state can be obtained as of Fe^{4+}, where the similar phenomenon can also be achieved 2IN6 model as of the dynamic charge transfer between Fe^{2+} and Fe^{4+}. By noting about such dynamic change of oxidation state, the local polarons induced by high oxidation state can further influence the reactivity such as CO reduction.

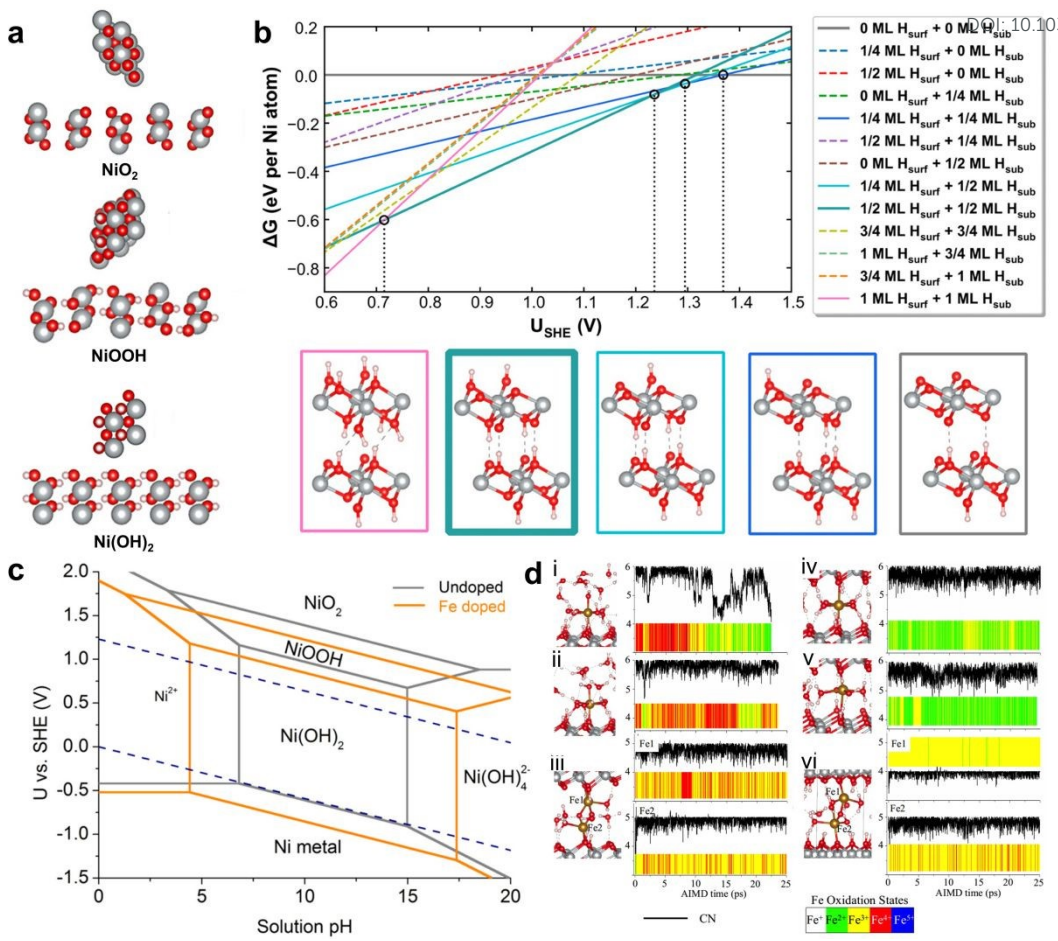

Fig. 3. (a-b) Schematic models for the phase transformation of $Ni(OH)_2$ and corresponding surface Pourbaix diagram with *H adsorbates.[77] Copyright 2024, American Chemical Society. (c-d) Comparison of Pourbaix diagrams for $Ni(OH)_2$ with and without Fe dopants, attached with the AIMD simulation result for dynamic change of $Ni(OH)_2$ with surface Fe species with various models: i. 3UP model, ii. 2UP model, iii. BRIDGE model, iv. 2IN6 model, v. 3IN6 model, vi. TILT model, respectively. The accompanied plots show the coordination numbers and oxidation states changed with the simulation time series.[78] Copyright 2020, American Chemical Society.

2.3. Construction of universal scaling relations

Heterogeneous catalysis includes the complex adsorption of various adsorbates over the solid surface, where the transformation of both stable species and transition states describe the catalysts surface states. As initialized by Hammer and Nørskov et al, the proposal of d-band theory reduced by the Newns–Anderson–Grimley model provides the basic prototype of linear correlation between adsorption energies of distinct adsorbates on metal surfaces[79, 80].

View Article Online
DOI: 10.1039/D6SC03404G

Consolidated by the d-band theory, Abild-Pedersen and Nørskov further disclose the term of scaling relation for describing energies of hydrogenation or dehydrogenation reactions for organic molecules over transition-metal surfaces with the assistance of density functional theory calculations[81, 82]. To be specific, the adsorption of molecule AH_x is determined to be linearly correlated with the adsorption energy of atom A in the simple format of $\Delta E^{AHx} = \gamma \Delta E^{A} + \xi$, where the slope γ is assumed to be affected by the valency of the adsorbate while the intercept ξ denotes the energy deviation. Beyond the constructed scaling relation based on the chemisorption energy, the construction of the Brønsted−Evans−Polanyi (BEP) relationships for surface reactions that describe the function between transition state energy (E_{TS}) and the reaction energy (ΔE), $E_{TS} = \gamma \Delta E + \xi$. As a result, with these universal scaling relations, the coupled ordinary differential equations based on rate theory from Langmuir−Hinshelwood−Hougen−Watson (LHHW) expressions can be solved to obtained the microkinetic property of the catalytic system. That is, the construction of universal scaling relations allows for the simple physical descriptor to describe the whole microkinetic property, largely decreasing the computation cost of DFT for complex heterogeneous catalysis systems. However, when it comes into the electrochemical reactions, owing to the driven effect from external bias potential, the redox behaviors induce the complex electron transfer within the Helmholtz layer that is hard to be treated in constant charge model[83, 84]. Therefore, the incorporation of electronic potential energy should be further considered beyond the intrinsic chemical reaction energy.

In terms of UOR process, the universal scaling relations were constructed by Lu et al over transition-metal (TM) pair atoms loaded on C_2N substrate (Fig. 4a) and Zhan et al over metal-doped CoS nanosheets (Fig. 4b) respectively.[85, 86] In detail, for the transition-metal pair atoms supported on C_2N substrate, two different pathways are considered including O_{ter} pathway and N_{ter} pathway, where the former pathway involves the adsorption of intermediates with O–TM interaction while the later pathway experiences the N–TM interaction (Fig. 4c). It is noted that the intermediate *CONHN was chosen as the key descriptor for interaction investigation between catalytic site and adsorbates. As shown in Fig. 4d, the adsorption of *CONHH presents the even end-on mode over Ni_2/C_2N substrate, where the symmetric metal atom pair allows the homogeneous adsorption mode with the medium transfer compared with $CrNi/C_2N$ and $CuNi/C_2N$ system. The linear regression in Fig. 4e states that the adsorption free energy of

View Article Online
DOI: 10.1039/D6SC03404G

*CONHN provides the strong correlation with *$CONH_2N$ with the format of ΔG(*$CONH_2N$) = 0.95ΔG(*CONHN) + 0.95, where the average R^2 value exhibits 0.90. For *CONN, the *CONHN also reveals the strong correlation of ΔG(*CONN) = 0.79ΔG(*CONHN) + 1.32, where the average R^2 value is assigned to be 0.97 (Fig. 4f). Beyond the adsorption energy as the descriptor in UOR, the integral crystal orbital Hamilton population (ICOHP) below the Fermi level can also be used. As shown in Fig. 4g, by noting about that the RDS in UOR is assigned to be the cleavage of C−N bond in urea, the ΔG_{RDS} obtained by the subtraction of the free energy of *NH from *urea-H shows the strong linear correlation with ΔICOHP defined by metal-nitrogen pair interaction, where the R^2 value is determined to be 0.996.

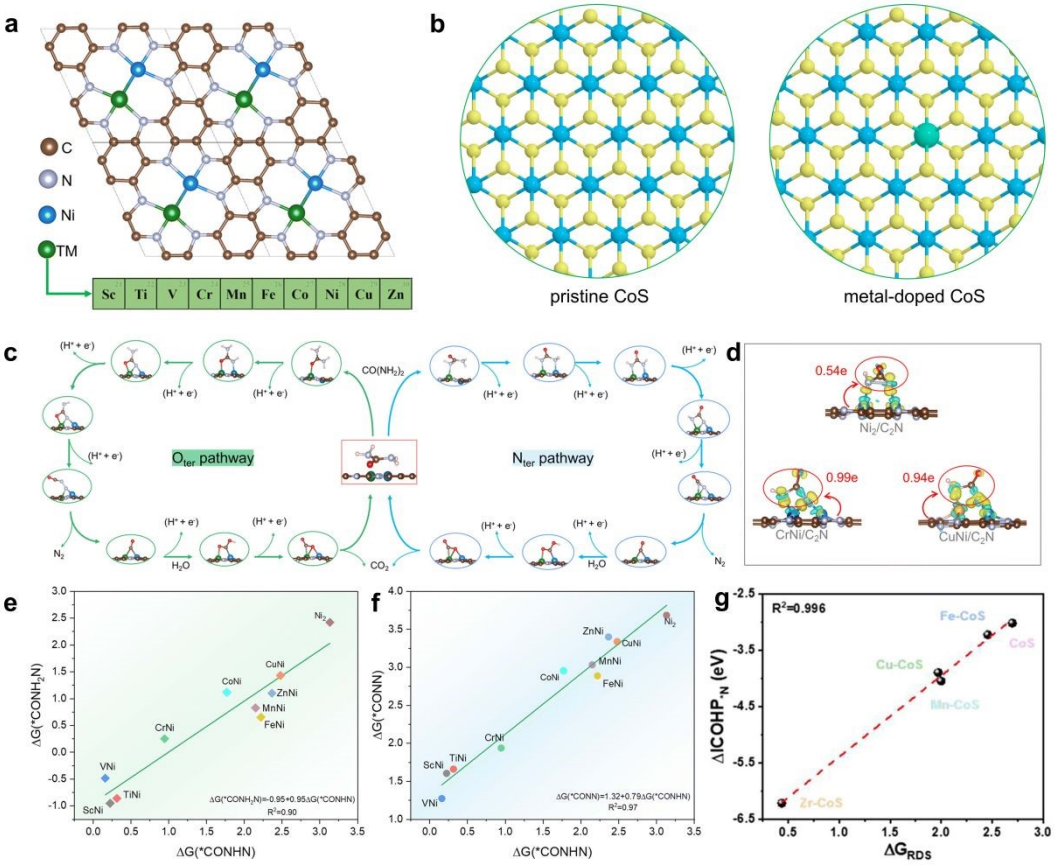

Fig. 4. (a) Schematic layer model for TM atomic pair loaded on C_2N substrate.[85] Copyright 2025, The Royal Society of Chemistry; (b) Schematic model of pristine CoS and metal-doped CoS model.[86] Copyright 2025, American Chemical Society. (c) The process of O_{ter} and N_{ter} pathway for UOR.[85] Copyright 2025, The Royal Society of Chemistry. (d) The charge density different for the adsorption of *CONHN with bader charge population.[85] Copyright 2025, The Royal Society of Chemistry. (e-f) Scaling relations of ΔG(*$CONH_2N$) and ΔG(*CONN) with ΔG(*CONHN).[85] Copyright 2025, The Royal Society of Chemistry.(g) Scaling relation

View Article Online
DOI: 10.1039/D6SC03404G

constructed by ΔICOHP and ΔG_{RDS} over metal-doped CoS system.[86] Copyright 2025, American Chemical Society.

3. Modulation types over nickel catalyst

3.1. Localized modulation of hetero-anion incorporation

As the typical two-dimensional material, $Ni(OH)_2$ usually exposes the low-coordinated surface sites to lead the electrocatalytic UOR process, while the strong on-site Coulomb interaction derived from the Ni *3d* shell suffers from the inferior electrical conductivity, limiting the expectation of large current density for electrochemical UOR. Taking *β*-$Ni(OH)_2$ as the example, Carter et al performed the insightful investigation over structural and electronic properties of *β*-$Ni(OH)_2$ and *β*-NiOOH based on first principles, where the formation of *β*-NiOOH is denoted as the deprotonation of *β*-$Ni(OH)_2$.[87] With the calculation of single-shot Green function (G_0W_0) for correction of notorious self-interaction and derivative discontinuity error, the band gap of *β*-$Ni(OH)_2$ and *β*-NiOOH are assigned with 5.83 eV and 1.96 eV respectively, stating that *β*-$Ni(OH)_2$ is a wide-gap insulator and *β*-NiOOH possesses the indirect gap as the semiconductor that guides the inferior electrical conductivity. Besides, the lowest energy state for *β*-NiOOH assumes the low-spin and antiferromagnetic configuration, where the low-spin d^7 state of Ni sites favors the Jahn-Teller distortion with the formation of two types of Ni−O bond length. Such distortion paves the basis for heteroatom incorporation for *β*-NiOOH to modulate the intrinsic property in meeting the operando condition of electrochemical UOR.

To improve the electrical conductivity and UOR performance of *β*-$Ni(OH)_2$, the surface sulfur incorporation in replace of O site presents the enhanced metallic property with effective electron transport by heating *β*-$Ni(OH)_2$ nanosheets under H_2S (Fig. 5a).[88] The sulfur incorporation into *β*-$Ni(OH)_2$ nanosheet can be viewed as the exchange between H_2O derived from the surface −OH group and H_2S molecule with −SH group. As shown in Fig. 5b, the overall formation of metallic $Ni(OH)_2$ experiences the exothermic energy change of 8.49 eV, where the protonation of surface −OH group into the release of H_2O is assigned with the larger downshift of energy along the reaction progress. After the sulfur incorporation, the metallic $Ni(OH)_2$ noted as M-$Ni(OH)_2$ exhibits the zero band contributed by the spin-down electronic

View Article Online
DOI: 10.1039/D6SC03404G

states in comparison with pristine $Ni(OH)_2$ as P-$Ni(OH)_2$, demonstrating the metallic property of M-$Ni(OH)_2$ (Fig. 5c). Consistently, M-$Ni(OH)_2$ nanosheets deliver the increased electrical resistivity with the enhancement of temperature, where such type of metallic behavior is determined to possesses the resistivity of 3.13×10^{-4} Ω·m under the room temperature with ultrahigh electrical conductivity (Fig. 5d). Additionally, M-$Ni(OH)_2$ also shows the electron concentration of ~10^{20} cm^{-3} with negative values of Hall coefficients, confirming the promotive role of sulfur incorporation for electrical transport of P-$Ni(OH)_2$ (Fig. 5e). Benefiting from the metallic property of M-$Ni(OH)_2$, the higher peak current density in 1 M KOH + 0.33 M urea is achieved with the contribution from urea compared with P-$Ni(OH)_2$, confirming the enhanced UOR performance of M-$Ni(OH)_2$ (Fig. 5f). Meanwhile, M-$Ni(OH)_2$ exhibits durable stability in charge transport and active site regeneration. With constant voltage analysis, M-$Ni(OH)_2$ delivers constant and high current density, along with a stable current response, while P-$Ni(OH)_2$ suffers obvious current attenuation. These results confirm that sulfur incorporation enhances the urea oxidation activity and operational stability of β-$Ni(OH)_2$, which is consistent with the mechanism analysis mentioned above. It should be noted that the poison effect by adsorption of CO_2 can also affect the catalytic performance beyond the high conductivity property. When NiOOH acting as the catalytic phase, the RDS during oxidation of urea is the desorption of CO_2 with the high energy barrier of 1.48 eV over P-$Ni(OH)_2$. In comparison, the energy barrier of RDS over M-$Ni(OH)_2$ states the lower value of 1.17 eV, suggesting that the sulfur incorporation can effectively alleviate the poison effect by CO_2 for favorable UOR performance (Fig. 5g).

View Article Online
DOI: 10.1039/D6SC03404G

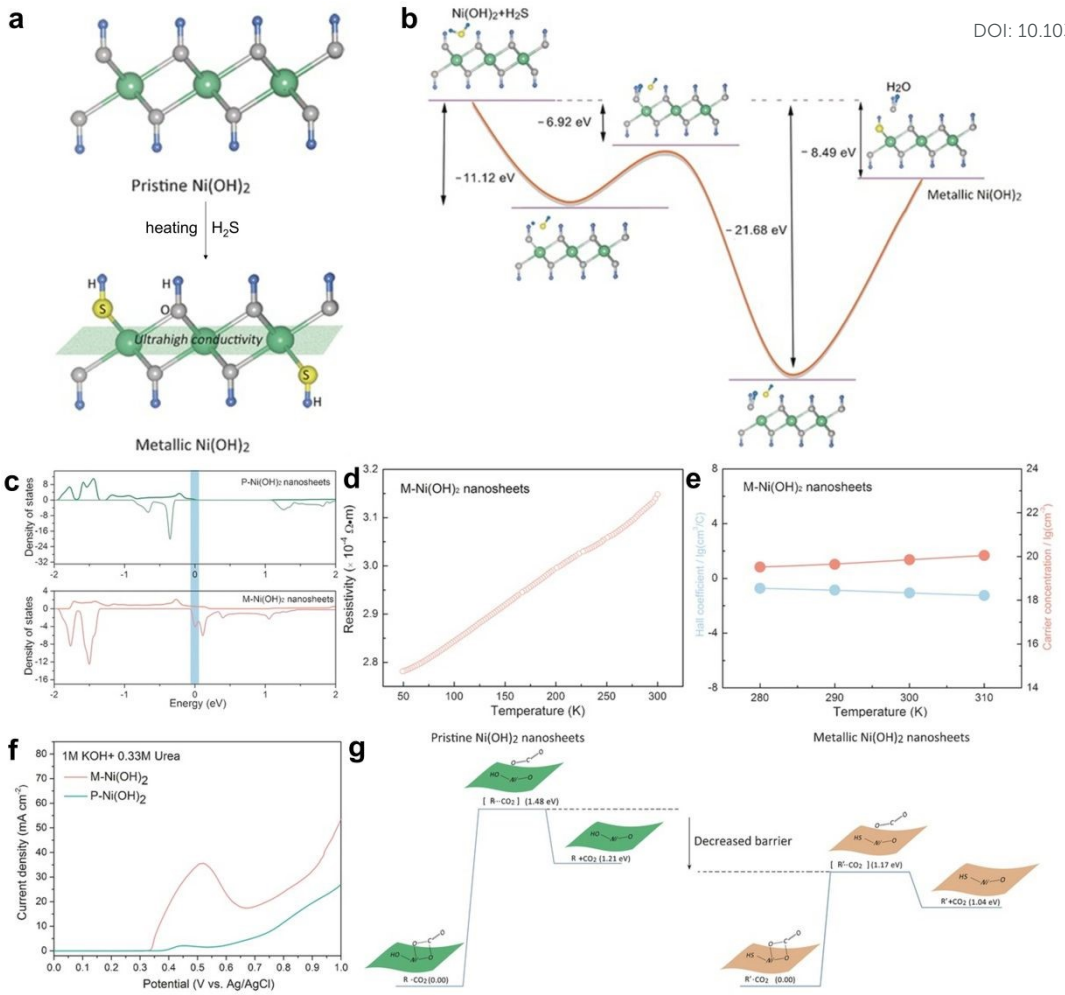

Fig. 5. (a) Synthetic process of M-Ni(OH)$_2$ with the S doping from heating H_2S; (b) Schematic process of reaction between H_2S and P-Ni(OH)$_2$ nanosheets to create the M- Ni(OH)$_2$; (c) Density of states (DOS) of P-Ni(OH)$_2$ and M-Ni(OH)$_2$; (d) Electrical resistivity of M-Ni(OH)$_2$ sample with the change of temperature; (e) Carrier concentration and Hall coefficient for M-Ni(OH)$_2$ sample. (f) Linear sweep voltammetry (LSV) curves for P-Ni(OH)$_2$ and M-Ni(OH)$_2$ samples in 1 M KOH + 0.33 M urea; (g) Energy profile for CO_2 desorption during UOR over P-Ni(OH)$_2$ and M-Ni(OH)$_2$. [88] Copyright 2016, Wiley-VCH GmbH.

Except for the strategy based on heteroatom incorporation, the inducement of anion vacancy also provides the modulation over nickel-based materials for electrochemical UOR. By referring to $NiMoO_4$ nanosheets (p-$NiMoO_4$) loaded on nickel foam (NF), Tong et al reported defect engineering strategy for abundant oxygen vacancy (r-$NiMoO_4$) serving as the highly-effective platform for UOR performance (Fig. 6a).[89] Compared with Ni foam, the growing of $NiMoO_4$ significantly enhances the UOR performance, indicating the catalytic

View Article Online
DOI: 10.1039/D6SC03404G

active phase. With the formation of oxygen vacancy in $NiMoO_4$, the lower onset potential and higher current density (249.5 mA cm^{-2}) are observed for r-$NiMoO_4$ compared with p-$NiMoO_4$ (130.5 mA cm^{-2}) (Fig. 6b). The DOS plot of r-$NiMoO_4$ (Fig. 6c) shows that the existence of oxygen vacancy downshifts the conduction band edge towards the Fermi surface related with p-$NiMoO_4$, illustrating the increased carrier concentration for promising transferring during oxidation process. Correspondingly, the charge transfer resistance (R_{ct}) measured by electrochemical impedance spectroscopy (EIS) determines the trend of p-$NiMoO_4$ (4.8 Ω) > r-$NiMoO_4$ (2.6 Ω), confirming the facilitated electron transferring for larger UOR current density of r-$NiMoO_4$ sample. Using the S−S bond as the electron transfer bridge, Ji et al reported the Co, V co-doped NiS_2 as the ternary synergistic system (NCVS) for electrochemical UOR. [90] Within the ternary system, it is hypothesized that the valence configurations of Ni^{2+}, Co^{2+}, V^{4+}, and V^{5+} are with $3d^8$, $3d^7$, $3d^1$, and $3d^0$, where the corresponding crystal field configurations are attached with $t_{2g}^6e_g^2$, $t_{2g}^5e_g^2$, $t_{2g}^1e_g^0$, and $t_{2g}^0e_g^0$, respectively. By noting about the partial occupancy t_{2g}/e_g orbitals, the Ni−S−S−V model in the ternary system equips Ni^{2+} with fully occupied t_{2g} state, which promotes the electron hopping towards V site with partial occupied t_{2g} state through S_2^{2-} bridge, defining the extended super-exchange interaction scheme for modulation the intrinsic property of Ni sites (Fig. 6d). In reference with the current density normalized by electrochemically active surface area (ECSA), the best NCVS-3 sample exhibits the largest current density, outperforming both of NCS-6 and NVS-1, thus confirming the vital role of ternary synergism effect. Within the NCVS system, the UOR pathway mainly follows the intermolecular N−N coupling with the captured $^{14}N^{15}N$ in 1 M KOH and 0.33 M urea [$CO(^{14}NH_2)_2$ + $CO(^{15}NH_2)_2$]. The proposed reaction route is revealed in Fig. 6e, where the V site acts as the electron extractor from Ni−Co pair to lead the electrooxidation of UOR. With the co-adsorption of urea molecule, the subsequent splitting of C−N bond leads the formation of CO and N_2 over Co and Ni site respectively, in which the further oxidation of CO into CO_3^{2-} produces the final products within the ternary system (Fig. 6f). Besides, with the incorporation of N into Ni_2P, Zhao et al reported the interfacial modulated N-Ni_2P as the active phase for electrochemical UOR.[91] It is shown in Fig. 6g that N-Ni_2P requires the lowest potential of 1.347 V_{RHE} to achieve the current density of 100 mA cm^{-2} compared with Ni_2P (1.375 V_{RHE}) and Pt/C (1.41 V_{RHE}), highlighting the most favorable kinetics. Notably, the NiOOH catalyst also presents the similar potential of 1.361 V_{RHE} as with N-Ni_2P despite the lower current density,

View Article Online
DOI: 10.1039/D6SC03404G

indicating that the oxidative reconstruction of Ni_2P into NiOOH is responsible for the active UOR performance. Using NiOOH as the active model, the free energy change in Fig. 6h states that the γ-NiOOH phase possesses the stronger thermodynamic driving feasibility than β-NiOOH in splitting of urea molecule into CO_2, where the RDS is assigned to be the desorption of $*CO_2$ derived from the energetics of ~1242.2 kJ/mol for the strong binding of Ni^{3+} site reported. Particularly, due to the dual adsorption of $*CONHNH_2$ over γ-NiOOH rather than the O-terminal mode over β-NiOOH, the susceptible nucleophilic attack by OH^- facilitates the C–N cleavage, where the subsequent N modulation towards the lower the adsorption of $*CO_2$ underscores the kinetic promotion of γ-NiOOH for highly active UOR.

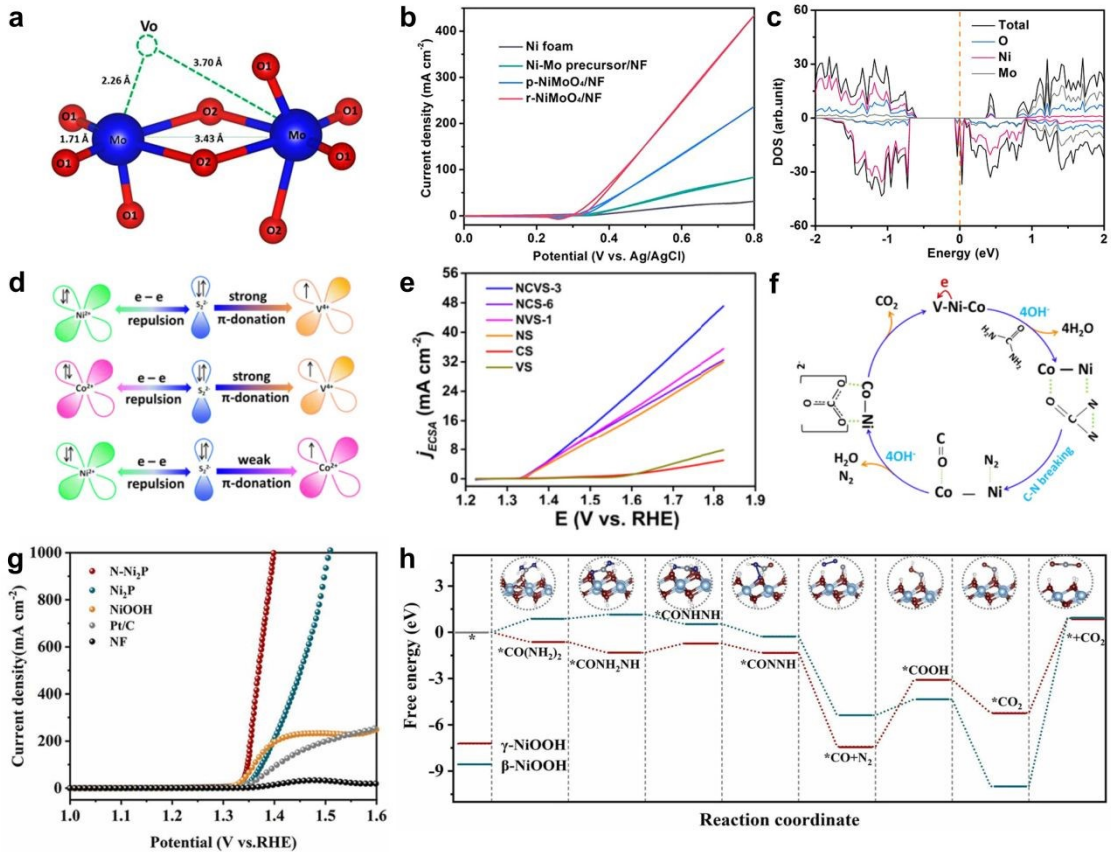

Fig. 6. (a) Schematic model of the oxygen vacancy over r-$NiMoO_4$; (b) Polarized cyclic voltammetry (CV) curves for $NiMoO_4$ samples; (c) DOS curves of oxygen-defect $NiMoO_4$.[89] Copyright 2017, American Chemical Society. (d) Schematic diagram for electronic coupling within Ni, Co, and V system. (e)Polarized curves over NCVS-included samples; (f) Proposed UOR mechanism over NCVS.[90] Copyright 2022, American Chemical Society. (g) LSV curves of Ni_2P system for UOR; (h) Free energy profile of urea splitting over β-NiOOH and γ-NiOOH.[91] Copyright 2026, Elsevier.

With the notation about the unique role of anion modulation, Geng et al discovered the highly-effective $Ni_2Fe(CN)_6$ catalyst by using –CN– as the bridge that connects the Ni and Fe sites for splitting the urea molecule.[92] At the current density of 100 mA cm^{-2}, the lower potential of 1.35 V_{RHE} is observed for $Ni_2Fe(CN)_6$, much smaller than the OER of 1.68 V_{RHE}. The satisfactory UOR performance of $Ni_2Fe(CN)_6$ is attributed to the stable Ni^{2+} with the avoidance for the formation NiOOH phase. Compared with $Ni_3[Co(CN)_6]_2$ and $Fe_4[Fe(CN)_6]_3$, the higher current density and lower potential are still obtained on $Ni_2Fe(CN)_6$, demonstrating the vital role of cooperative interaction within Ni–CN–Fe site (Fig. 7a). By changing the urea concentrations in KOH electrolyte, $Ni_2Fe(CN)_6$ shows the urea-independent behavior as similar with most of Ni-based catalysts, where the slope of scaling relation between log$j$ and logC_{urea} is calculated to be 0.18 (Fig. 7b). Differently, with the changing of KOH concentrations, $Ni_2Fe(CN)_6$ discloses the strong dependence (slope of 1.10) with respect to the OH^- concentration, where such pH dependence versus onset potential is determined to be ~59 mV/pH, denoting the typical Nernstian-type behavior for the single H^+/e^- coupled RDS (Fig. 7c). The UOR pathway is proposed to include two stages of chemical splitting of urea into CO_2 + NH_3 ($CO(NH_2)_2 + H_2O \rightarrow CO_2 + 2NH_3$) and the oxidation of NH_3 into N_2 ($2NH_3 + 6OH^- \rightarrow N_2 + 6H_2O + 6e^-$), where the Ni and Fe sites take different catalytic processes. As shown in Fig. 7d, at the first stage of urea splitting, the Ni site exhibits the more favorable transformation of *$OCONH_2$ into *NH_2 and CO_2 with the lower free energy change (0.90 eV) compared with Fe site (1.02 eV). The reaction dynamics in Fig. 7e also supports the active trend for the C–N cleavage of Ni > Fe, where the Ni site presents the lower activate energy of 1.38 eV. In terms of the second stage, the Fe site facilitates the deprotonation of *NH_2 into *NH as the RDS, where the lower free energy change of 0.92 eV is assigned for Fe site compared with the Ni site of 1.20 eV. The corresponding activation energy also suggests the lower value of 1.29 eV (Fe site) related with Ni site (1.33 eV) (Fig. 7f), confirming the promoted deprotonation kinetics for subsequent intermolecular N–N coupling at Fe site. Similarly, Zhao et al also reported the cyanide-bridged Ni-Fe bimetallic catalyst as $Ni_2Fe(CN)_6$ for efficient UOR.[93] In their work, it is noted that the cyanide bridge serves as the electron transfer medium, supplying the stable Ni^{3+}/Ni^{2+} redox shuttle with linked Ni and Fe sites. The synergism with the unique Ni–CN–Fe site assisted by the adsorption of *OH undergoes the advantageous consecutive

View Article Online
DOI: 10.1039/D6SC03404G

dehydrogenation, thus promoting the multi-pathway for urea splitting.

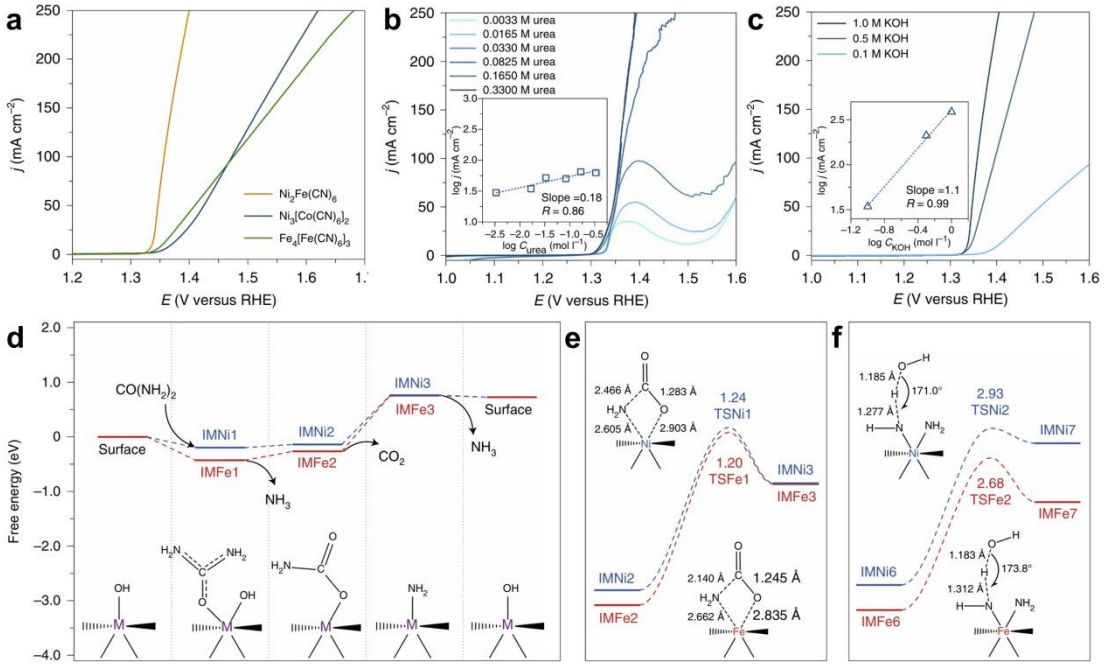

Fig. 7. (a) Polarized LSV curves of distinctive nickel ferrocyanide catalysts in 1.0 M KOH that contains 0.33 M urea; (b) LSV curves of $Ni_2Fe(CN)_6$ in 1.0 M KOH with different urea concentrations; (c) Comparison of UOR and OER performance; (d) Gibbs free energy profile of the UOR at the first stage; (e) The activation energy profile of C–N cleavage; (f) The activation energy profile of $*NH_2$ deprotonation.[92] Copyright 2021, Springer Nature.

3.2. Localized modulation from metal cation with closed shell

Assuming the active phase of $Ni(OH)_2$ or NiOOH for electrochemical UOR, the modulation for the Ni site also shares the vital role that the changing of geometric structure brings about the contribution both from electronic structure and topology effect, which is able to further tune the adsorption behavior of intermediates. As indicated in the electronic structure of $Ni(OH)_2$, the localized *3d* shell possesses the strong on-site Coulomb interaction within the coordination with lattice O, thus necessitating the re-comprehension over the band structure theory. From the chemist's view, the band structure of six-fold metal-oxygen (M–O) coordination comprises the simple *3d-2p* orbital overlap, producing the formation of bonding (M–O) band and antibonding (M–O)* band separately (Fig. 8a).[94] Depending on the electronegativity difference between M and O, the energy gap between (M–O) and (M–O)* band is defined as the charge transfer term Δ_{CT}. In terms of the Li-rich materials, the negligible overlap between Li *2s* and O

2p orbitals leads to the increased degree of involvement of lattice oxygen atoms in thermal motion, which creates the additional non-bonding O states, also known as b_1* state in C_{2v} symmetry. The Lewis configuration of O^{2-} ion is comprised of one *2s* ($|O_{2s}$) and three *2p* ($|O_{2p}$) orbitals, the hybridization being typically sp^3 format with countable electron lone pairs as the nucleophilic site. Cationic substitution provides the effective strategy to increase the number of $|O_{2p}$ electron lone pairs. With the incorporation of metal species with closed valence shell such as alkali, alkali earth or $3d^{10}$ series into transition-metal-based oxides (TMOs), the degree of covalency involvement for TM site can be largely reduced, as indicates by the accumulated electron localization function distribution around the Li and Na site, which is contributed by the $|O_{2s}$ and $|O_{2p}$ orbitals. With the cationic vacancies derived from the leaching of Li^+, Na^+, and Mg^{2+} species, the anionic redox can be activated, which can be confirmed by the electron localization function (ELF) around the O lattice O sites (Fig. 8b).[95] During the charging process such as oxidation reaction, the electron loss from lattice O *2p* states creates the oxygen holes (h^O), resulting in the topological disordering at high number of h^O for the formation of dimerization beyond the interaction within *3d-2p* orbital overlap (Fig. 8c), where the location of O–O dimerization is assigned with the O–O π* above the Fermi level.[96]

View Article Online
DOI: 10.1039/D6SC03404G

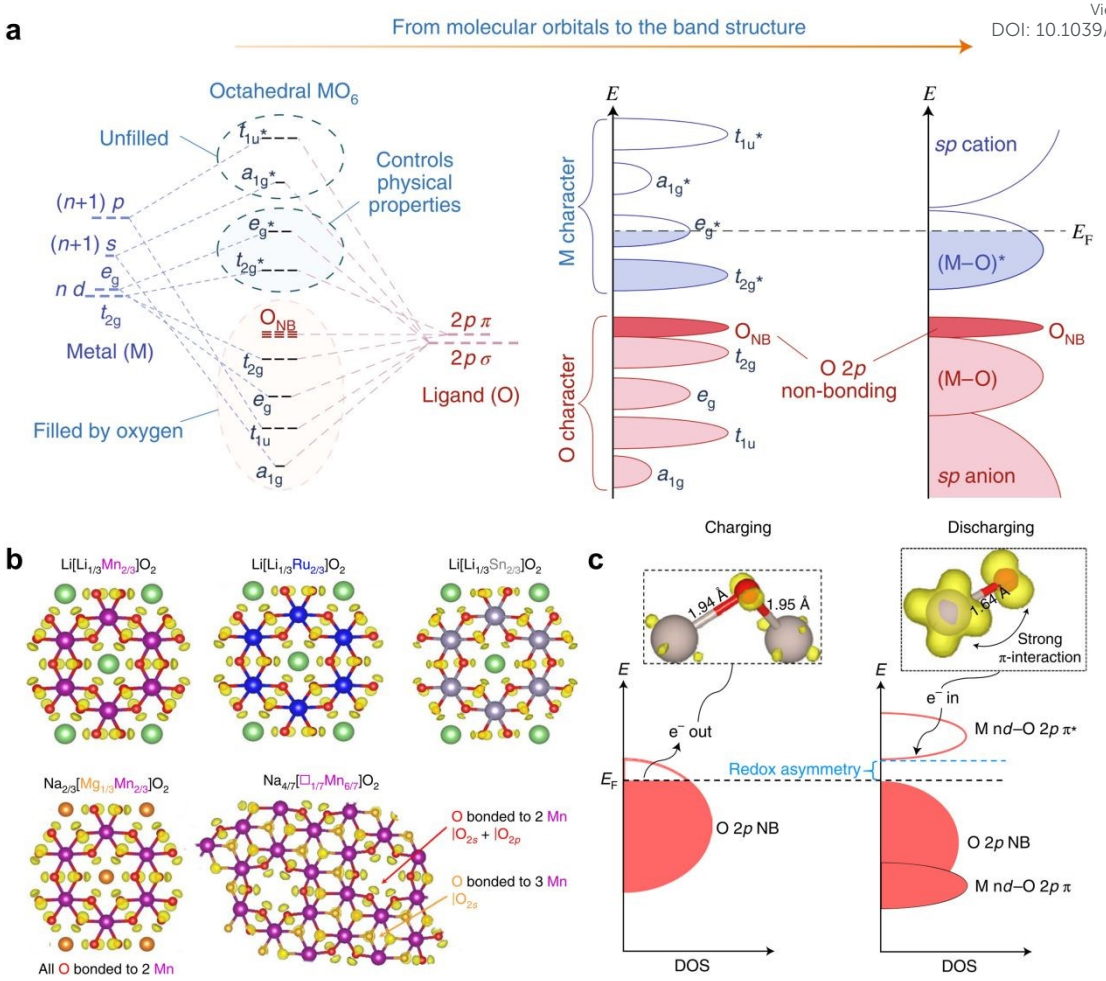

Fig. 8. (a) Quantitative molecular orbital diagram with conventional band-structure of transition-metal oxides.[94] Copyright 2018, Springer Nature. (b) ELF diagrams obtained from first-principle calculations for $Li[Li_{1/3}M_{2/3}]O_2$ (M=Mn, Ru, Sn).[95] Copyright 2019, Springer Nature. (c) Schematic diagram of charging process for cation with strong TM–O π hybridization.[96] Copyright 2022, Springer Nature.

However, beyond the contribution of non-bonding O *2p* states, the removing of electrons from the mixed non-bonding O *2p* and (M–O) bands can also avoid the risk of structural destabilization, denoting the complex components within the (M–O)* band. To understand such behavior, the *d*–*d* Coulomb interaction term U should be considered beyond the Δ_{CT} term, where the insight of Mott-Hubbard splitting for correcting the failure of one-band view is typically not sketched by chemists but by solid-state physicists. In the Mott-Hubbard scheme, the splitting of (M–O)* band forms the occupied lower Hubbard band (LHB) and the empty upper Hubbard band (UHB). Depending on the competition between U and Δ_{CT} term, the electron

loss during charging process determines the ion redox property including the reversible structural distortion with O–O dimerization ($U/2 \approx \Delta_{CT}$) and irreversible release of O_2 with completely structural distortion ($U >> \Delta_{CT}$) (Fig. 9a). One thing should be noted that the band position of non-bonding O *2p* states largely affects the ion redox behavior within the Mott-Hubbard splitting scheme. The accumulation of O *2p* states can be captured by adding the number of metal cations with closed shell (e.g. Li^+), in which the increased DOS of O *2p* around the energy level of -1.5 eV in Figure 9b for the Li–O–Li configuration confirms the non-bonding property that activates the degree of covalency involvement (Fig. 9b).[97] Similarly, such activation of non-bonding states can also be determined from the π[Mn–O] system (e.g. $Na_4Mn_6O_{14}$), as analyzed by Kitchaev et al.[98] As shown in Fig. 9c, the π system presents the D_{3d} symmetry, comprising two subsystems contributed by Mn-*d* and O-*p* orbitals, where the single *d* orbital in the Mn site reveals the non-bonding t_{2g} level in octahedral MnO_6 structure while the *p* orbital in O site provides the indirect σ bonding. With the symmetry-adapted linear combination of D_{3d} group orbital sets, the total energy level diagram splits into a_{1g}, e_u, e_g, a_{2u}, a_{1u} and their corresponding antibonding states, in which the non-bonding states are composed of a_{2u} from O site and a_{1u} from metal site. By projection of DOS over Mn and O sites, the predicted π states originate from non-bonding t_{2g} and e_g* states in the MnO_6 environments, where the highest occupied molecular orbital (HOMO) is assigned to be the anti-bonding e_g* state. As a result, the delocalized π[Mn–O] bonding condition creates the high-energy e_g* level, being electrochemically active during the charging process for structural distortions derived from the formation of oxygen dimers.

View Article Online
DOI: 10.1039/D6SC03404G

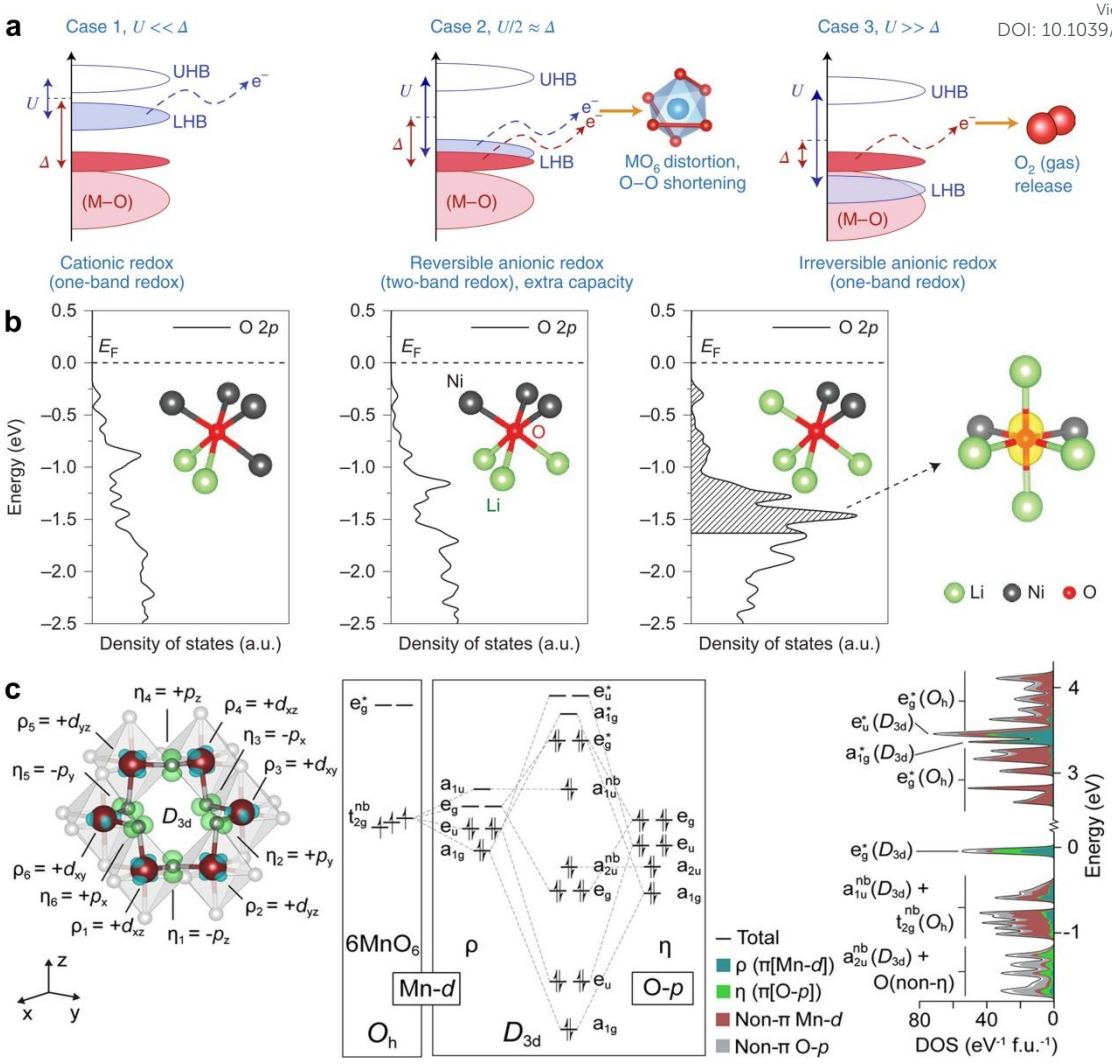

Fig. 9. (a) Schematic diagram of consideration of Mott-Hubbard splitting in the ion redox behavior during charging process.[94] Copyright 2018, Springer Nature. (b) Gradual changing of O *2p* states in the $LiNiO_2$ system, with the labile O *2p* observed in the particular Li–O–Li configuration.[97] Copyright 2016, Springer Nature. (c) Symmetry analysis for D_{3d} with π[Mn−O] redox center, the derived molecular orbital levels, and the projection of the $Na_4Mn_6O_{14}$ G_0W_0 DOS diagram.[98] Copyright 2021, American Chemical Society.

Concerning the role of nucleophilic attack from lattice O site, Han et al reported the cationic vacancy controllable $LiNiO_2$ (LNO) model catalyst for electrochemical UOR.[99] By chemical delithiation method, various LNO-x catalysts were achieved with the specific ratio between Li and NO_2BF_4. As shown in Fig. 10a, the octahedral (O_h) NiO_6 structure presents the orbital components of a_{1g}, t_{1u}, e_g, t_{2g} and their anti-bonding states, in which the O t_{2g} states

contributed by O sites guide the non-bonding area. Due to the absence of the interaction between Li and O, the electron density is accumulated onto the lattice O site for LNO-2 with higher ratio of delithiation, denoting the activation of lattice oxygen (Fig. 10b). To be specific, the Ni^{2+} $3d^8\underline{L}$ configuration denotes the $t_{2g}^6e_g^2$ term, while Ni^{3+} $3d^7\underline{L}$ configuration is noted as $t_{2g}^6e_g^1$ term. Benefiting from the Mott-Hubbard splitting, the charge unbalance derived from delithium creates the rearrangement of electron density around the band edge below the Fermi level, leading the formation of new non-bonding O bands (Fig. 10c). As a result, the downshifted LHB induced by the hybridization between Ni^{4+}-t_{2g} orbitals and O *2p* band provides the mixing with non-bonding O *2p* states, delivering the two-band redox behavior during oxidation conditions. With the addition of urea into 1 M KOH electrolyte, the LNO-2 sample presents the sharply increased current density, which confirms the catalytic activity for the response of electrochemical UOR behavior (Fig. 10d). After the 1000 cycles, the increase in anodic current density of 1.25 mA cm^{-2} with positive shift the peak potential is displayed in comparison with the initial cycle, confirming the well-behaved durability of LNO-2 sample, as shown in Fig. 10e. Concerning the activation of lattice oxygen of LNO, the most stable adsorption configuration of urea molecule is determined to be the bridge coordination between C and lattice O, where the lattice O behaves as the nucleophilic site. As shown in Fig. 10f, the distinction between AEM and LOM pathway for LNO-0 is assigned to be coupling between *$CONNH_2$ and lattice oxygen to form the oxygen vacancy. Compared with the deprotonation of *$CONNH_2$ into *CONNH via AEM pathway, such deprotonation with the formation of oxygen vacancy is exothermic via LOM pathway, denoting its thermodynamic advantage. With the delithium, the LNO-2 sample shows the facilitated electrochemical deprotonation for the urea molecule along with the accelerated electron transfer. Within the LOM pathway, the LNO-2 sample reveals the favorable intramolecular N–N coupling with the release of CO_2 and N_2. After the electrochemical transformation of urea with the sacrifice of oxygen vacancy, the recovery of OH^- into the vacancy completes the catalytic loop for LNO-2.

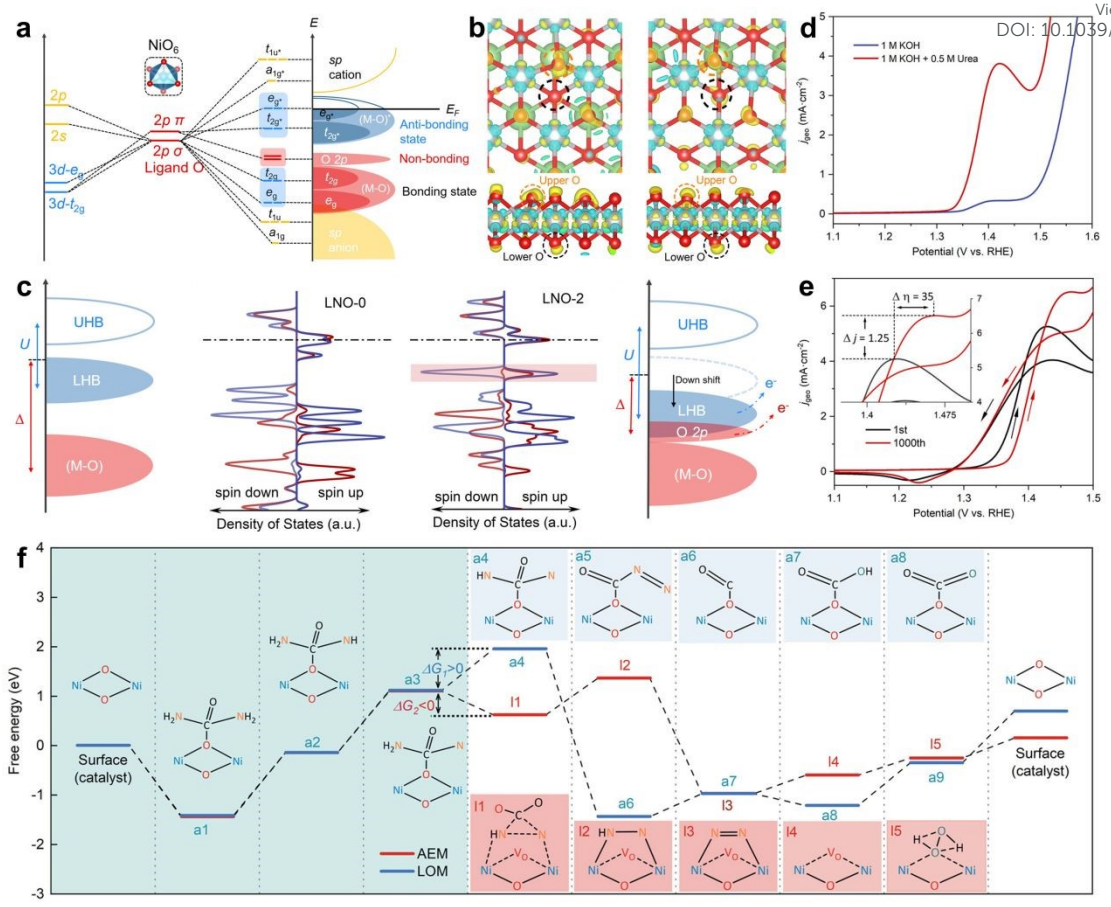

Fig. 10. (a) Qualitative molecular orbital diagram for octahedral of NiO_6 structure; (b) Charge density difference of LNO-0 and LNO-2 respectively; (c) Diagram of Mott-Hubbard splitting in LNO system with PDOS profiles of LNO-0 and LNO-2; (d) LSV curves of UOR for LNO-2; (e) Polarization curves before and after 1000 cycles for LNO-2; (f) Comparison of the free energy profiles between AEM and LOM pathway during UOR for LNO-0.[99] Copyright 2022, Wiley-VCH GmbH.

3.3. Localized modulation from transition metal

By noting about the insight from the band structure theory above, the unique interaction within d electrons shares the vital role in modulation of electrochemical UOR. With the incorporation of tungsten (W) into nickel catalyst, Wang et al reported the highly-effective Ni-WO_x catalyst for electrochemical UOR.[100] As shown in Fig. 11a, the Ni-WO_x sample requires the lower potential of 1.40 V to reach the larger current density of 100 mA cm^{-2}, presenting the downshifted 273 mV potential related with OER. Concerning the advantage of UOR in replace of OER, the electrochemical performance was further applied in a flow electrolyzer (Fig. 11b).

With the assistance of cathodic CO_2 reduction, the electrochemical performance only needs the cell potential of 2.16 V to operate at the current density of 100 mA cm^{-2} for formation of CO and urea spitting, which is significantly lower than the use of OER as the anodic reaction (downshift of 370 mV) (Fig. 11c). It is concluded that the well-behaved UOR performance originates from the unique electron transfer between W and Ni atoms within Ni-WO_x. With the occurrence of UOR over the directly exposed Ni site, the adsorption of C=O group mainly locates at the negatively charged region (Ni site), while the amino group $-NH_2$ prefers the adsorption over W site, thus favoring the splitting of urea molecules through polarization (Fig. 11d). Similarly, Liu et al proposed the self-supported W-doped Ni-$C_3S_3N_3$ coordination polymer (W-NT) as the highly-effective catalyst for electrochemical UOR.[101] With the tailoring of active Ni^{3+} site via ligand anchoring and high-valence metal doping, the lower potentials for driving UOR only require 1.39 V and 1.43 V at the current densities of 50 mA cm^{-2} and 100 mA cm^{-2}, compared with OER outcome of 1.63 V and 1.71 V. The lowering of d-band center for Ni site with the doping of W confirms the chemical reduction tendency, which helps the stabilization of appropriate valence state of Ni^{3+} site and the optimization the adsorption strength towards urea molecule (Fig. 11e). Benefiting from the W doping, the Ni^{3+} reveals the preferrable adsorption energy of -0.70 eV for urea molecule compared with H_2O of -0.29 eV, denoting the favorable capture of urea for consecutive transformation (Fig. 11f). During the electrochemical UOR progress, the potential determining step (PDS) is assigned to be the deprotonation of *NH_2NH_2 into *$NHNH_2$ with the energy gap of 0.83 eV, significantly lower than the PDS of formation of *OHOH in OER (1.71 eV). Besides, the construction of dual active site of Ni-WO_3 is also discovered to regulate the adsorption of *COO intermediate for urea splitting.[102] Benefiting from the electron transfer from Ni to WO_3, the adsorption of urea exhibits the dual binding of $-NH_2$ group and C=O group over Ni and WO_3 simultaneously, where such bridge adsorption mode of Ni−NCO−W lowers the C−N cleavage barrier, promoting the consecutive transformation of *COO over WO_3 site and the formation of N_2 at Ni site, enabling the coupled desorption of CO_2 and N_2 effectively. With the construction of Ni–O–Mn unit site, Sun et al reported the highly-effective self-supported NiMn metal organic framework (NiMn-MOF) loaded with ultrafine Pt nanocrystals as Pt_{NC}/NiMn-MOF for

electrochemical UOR.[103] Within the Ni–O–Mn unit site, the electronic repulsion in high-spin Ni–O enhances the π-symmetry between Mn^{3+} and O^{2-}, which favors the electron transfer throughout the catalyst. The introduction of Pt_{NC} further regulates the charge redistribution, thus optimizing the chemisorption behavior to reduce the energy barrier of RDS.

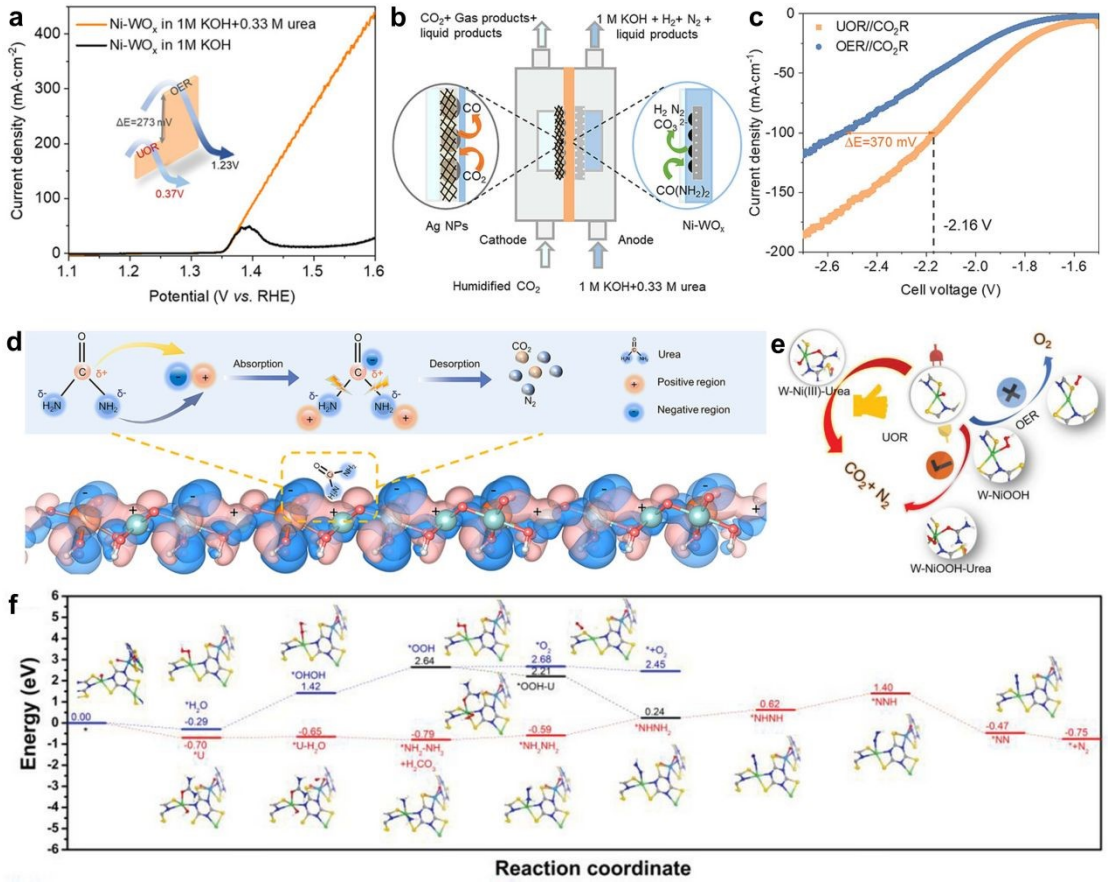

Fig. 11. (a) Comparison of polarization curves for Ni-WO_x with and without 0.33 M urea; (b) Schematic image of coupling between UOR and CO_2R for cell electrolyzer; (c) Polarizations curves for the UOR|CO_2R electrolyzer compared with OER|CO_2R; (d) Adsorption mode of urea over Ni-WO_x with calculated charge density difference.[100] Copyright 2021, Wiley-VCH GmbH. (e) Proposed mechanism of UOR over W-NT system; (f) Free energy profile of W-NT in terms of UOR and OER.[101] Copyright 2023, Wiley-VCH GmbH.

By noting about the unique role of W, Cat et al also reported the construction of single-atom W doped nanoporous P–$Ni(OH)_2$ catalyst as np/W–P–$Ni(OH)_2$ to lead the chemical-electrochemical coupled pathway for UOR.[104] As shown in Fig. 12a, the conventional pathway for Ni-based catalysts follows the self-oxidation reaction to create the NiOOH phase, allowing

for the formation of key intermediates including *CONHN, *CON_2, and so forth, where the RDS is assigned to the formation of CO_2 with the higher overpotential. Differently, with the proceeding of chemical-electrochemical coupled pathway, np/W–P–$Ni(OH)_2$ enables the almost thermoneutral lattice hydroxyl dehydrogenation of $Ni(OH)_2$ to form the Ni(OH)O phase, thus leading the highly-effective pathway with the low energy barrier. As revealed by the high-angle annular dark-field scanning transmission electron microscopy (HAADF-STEM) image, the np/W–P–$Ni(OH)_2$ presents the core-shell-like morphology with the atomic distribution of W in the shell (Fig. 12b). With the electrochemical measurement in 1 M KOH with 0.33 M urea, the np/W–P–$Ni(OH)_2$ sample shows the lowest Tafel slope of 52.6 mV dec^{-1}, demonstrating the most favorable kinetic process of UOR (Fig. 12c). The practical display in hydrogen production with the coupled UOR system further states the decreased cell potential of 316 mV, compared with the OER performance, thus denoting the promising application (Fig. 12d). To unveil the dynamic kinetics of UOR, potential-dependent Bode plots in Fig. 12e exhibit that the doping of W into np/P–$Ni(OH)_2$ shifts the phase peak of urea oxidation towards higher frequencies, which is indicative of the enhanced electron transfer property. With the notation about W-induced favorable kinetics, the calculated PDS of W–P–$Ni(OH)_2$ is the adsorption of urea with the free energy change of 1.176 eV, lower than the PDS of the dehydrogenation of urea into *$CONHNH_2$ (1.94 eV) for pure $Ni(OH)_2$, as shown in Fig. 12f. After the formation of *NH_2 (Fig. 12g), the subsequent PDS for W–P–$Ni(OH)_2$ is the deprotonation of *NHOH into *NHO with the free energy gap of 1.045 eV, lower than the PDS of pure $Ni(OH)_2$ as the deprotonation of *NHO into *NO. Beyond the incorporation of W, some commonly used transition metals have also exerted analogous modulation effects. Xie et al developed electron-delocalized Ni–Co active pairs to achieve efficient UOR performance by doping Co into $Ni(OH)_2$ and integrating with CoNi alloy.[105] Electron delocalized Ni–Co sites within catalyst lead to the upshifted d-band center, orbital hybridization and electron transfer between the electron delocalized Ni–Co sites and the N atoms in urea are significantly enhanced, which decreases the electron transfer from H to N in the N─H bond and weakens the N─H bond. Demonstrated by in-situ characterizations and theoretical investigation, the RDS of UOR is *$CONH_2NH_2$→*$CONH_2NH$, the $Ni^{2+\delta}$–O–$Co^{2+\delta}$ delivers a rate-determining step with an

View Article Online
DOI: 10.1039/D6SC03404G

energy barrier reduced to 1.58 eV, far superior to that of pure $Ni(OH)_2$.

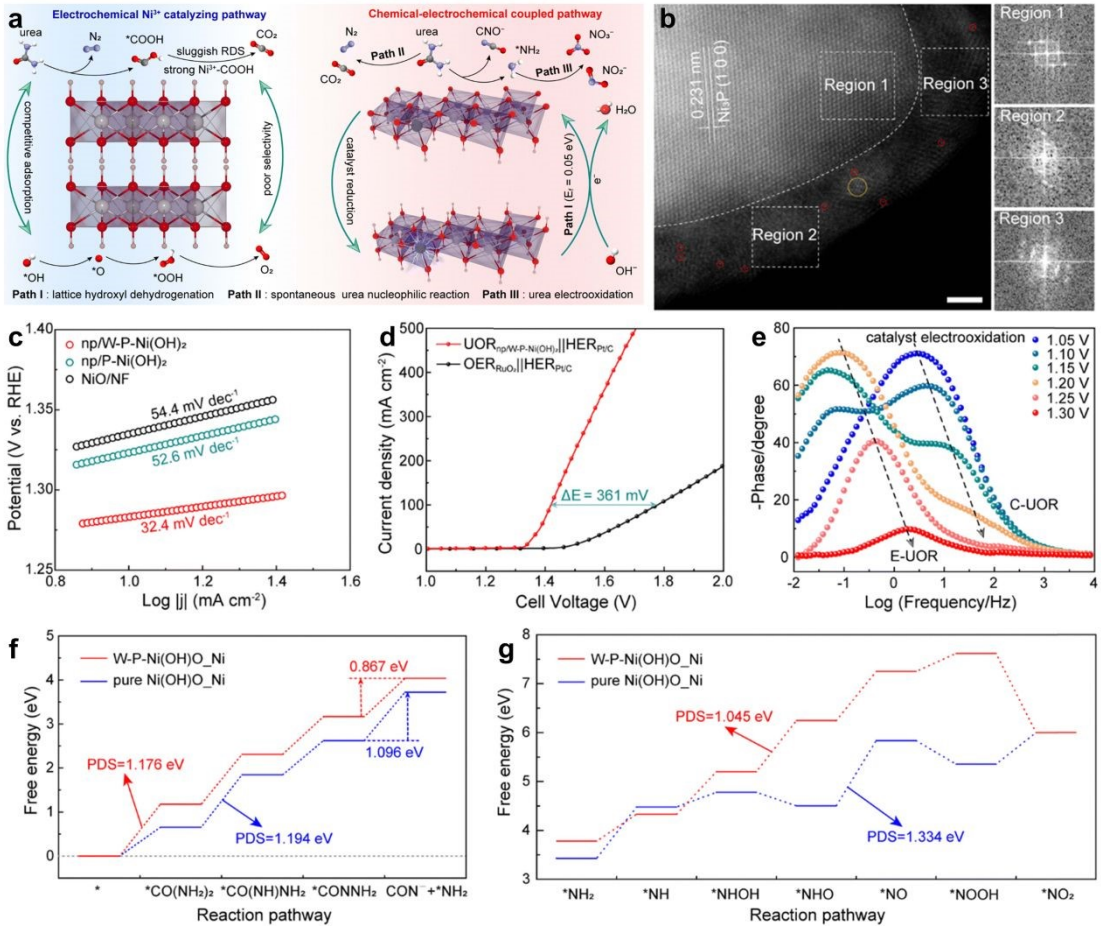

Fig. 12. (a) Schematic diagram of various UOR pathways; (b) The HAADF-STEM image of np/W–P–$Ni(OH)_2$ sample; (c) The calculated Tafel plots for electrochemical UOR; (d) The overall performance of hydrogen production via UOR||HER system; (e) Potential-dependent Bode plots of np/W–P–$Ni(OH)_2$ for UOR; (f-g) Free energy profiles of pure Ni(OH)O and W–P–$Ni(OH)_2$ along the UOR progress.[104] Copyright 2025, The Royal Society of Chemistry.

To realize the transformation of urea into innocuous N_2 for sustainable goal rather than the formation of NH_3 as the acidic rain resource, Zhan et al proposed the atomic anchoring Ni over Ti foam system with the synthesis of asymmetric Ni–O–Ti site.[106] As shown in Fig. 13a, it is observed that the atomic Ni site is distributed onto the surface of the TiO_x substrate, where the atomic dispersion is further intensified via the elemental mapping. With the determination of coordination environment of the asymmetric Ni–O–Ti site (Fig. 13b), the Fourier-transformed extended X-ray absorption fine structure spectroscopy (FT-EXAFS) exhibits the characteristic

peak at 1.59Å of Ni–O shell, where the absence of Ni–Ni coordination further confirms the atomic dispersion of Ni site into TiO_x. During the electrochemical UOR process, the asymmetric Ni–O–Ti sites disclose the low potentials of 1.30 V and 1.33 V for the current densities of 10 mA cm^{-2} and 100 mA cm^{-2} respectively. Meanwhile, Ni–O–Ti sites exhibit a Tafel slope of only 14.2 mV dec^{-1}, notably smaller than 20.0 mV dec^{-1} for Ni–O–Ni sites and 20.8 mV dec^{-1} for Ni foam. All the electrochemical performance outperforms both of symmetric Ni–O–Ni sites and Ni foam. Within a potential range of 1.40 to 1.70 V, Ni–O–Ti sites still maintain a selectivity of 99 % for N_2 evolution, which is consistent with the electrochemical performance result mentioned above. By feeding the equivalent ratio of $CO(^{14}NH_2)_2$ and $CO(^{15}NH_2)_2$, the observed mass spectral distribution in online mass spectrometry witnesses the $^{14}N_2$:$^{15}N_2$:$^{14}N^{15}N$ ration of 1:1:0, indicating the dominant intramolecular N–N coupling over asymmetric Ni–O–Ti sites (Fig. 13c). For clarification of the electrochemical UOR pathway over asymmetric Ni–O–Ti sites, the *in situ* FTIR spectroscopy in Fig. 13d delivers that the adsorption of urea onto asymmetric Ni–O–Ti site demonstrates the blueshift of ν_a(C═N) mode compared with that onto Ni–O–Ti site, stating the strengthening of C═N bond. Concerning the oxophilicity of Ti site, such chemisorption of urea can be accounted by the unique configuration of C=O→Ti format. The lack of peaks attributed for NCO^- or NO_x^- over the asymmetric Ni–O–Ti site throughout all the bias potentials determines the high N_2 selectivity as the clean products. As shown in Fig. 13e, the urea adsorption over Ni–O–Ti manifests the obvious electron accumulation for two C═N bonds, which accounts for the facilitated interactions of C=O group in comparison with Ni–O–Ni site. Upon the adsorption of urea on asymmetric Ni–O–Ti site, the intramolecular N–N is favored during the initial deprotonation process with the energy change of 0.41 eV, while the breaking of C═N bond involves the higher energy change of 1.03 eV (Fig. 13f). The production of N_2 with the minor energy change (0.13 eV) via the subsequent deprotonation accounts for the high selectivity for N_2 product.

View Article Online
DOI: 10.1039/D6SC03404G

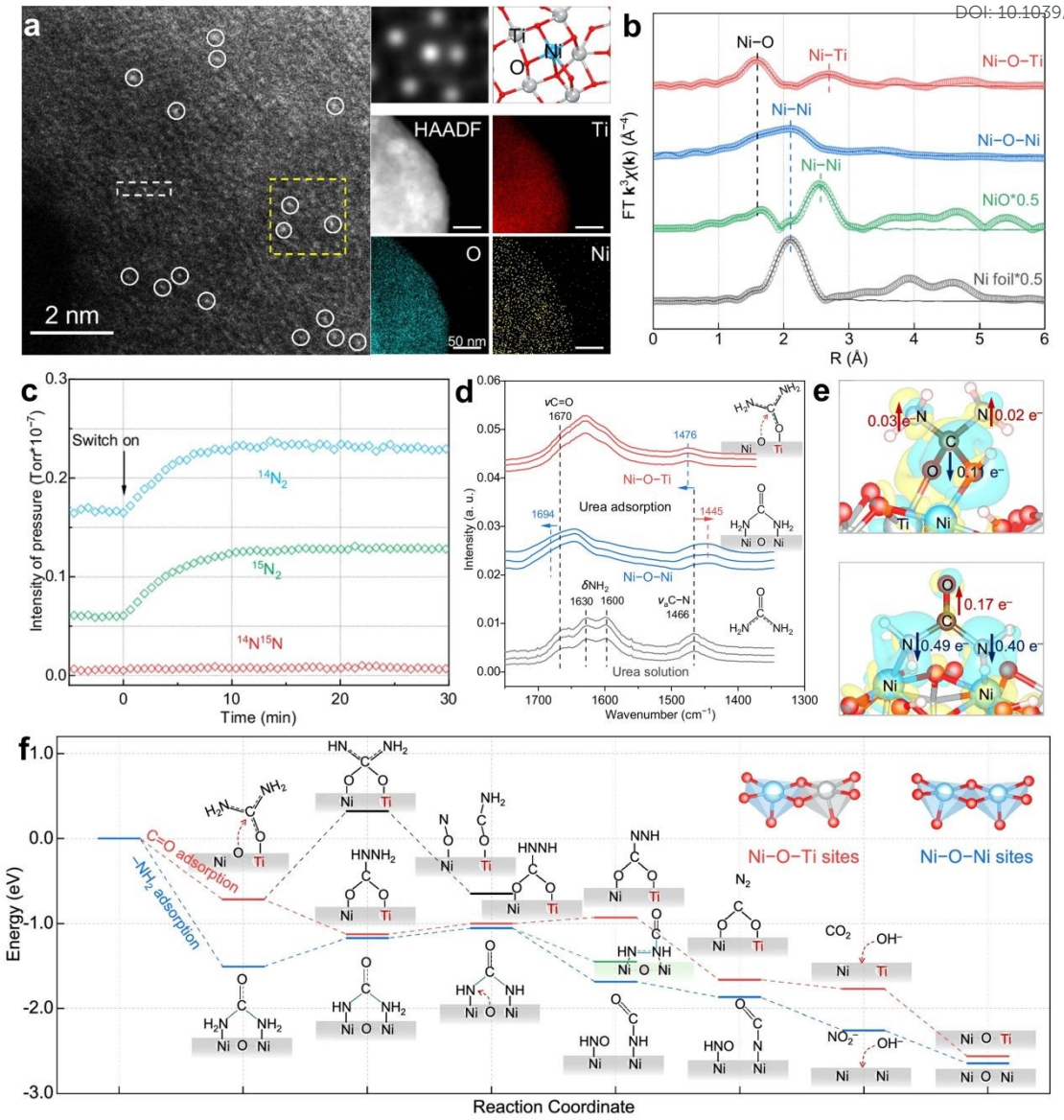

Fig. 13. (a) Aberration-corrected HAADF-STEM image for Ni–O–Ti site with marked Ni site and elemental mapping; (b) FT-EXAFS spectra for Ni–O–Ti site; (c) N_2 contents determined by online mass spectroscopy over asymmetric Ni–O–Ti site; (d) The *in situ* FTIR spectra for electrochemical UOR process with the changing of bias potential; (e) Charge density differences for adsorption of urea over Ni–O–Ti site and Ni–O–Ni site; (f) Free energy profile for UOR progress on asymmetric Ni–O–Ti and symmetric Ni–O–Ni sites. [106] Copyright 2024, Spinger Nature.

3.4. Localized modulation from rare earth dopants

The rare-earth species are comprised of Sc, Y, and the whole lanthanide series (ranging from La to Lu), revealing similar physical and chemical properties. The beauty of rare-earth species

lies in that the subtle quantity alters the material property, which are capable of serving as the vitamin dopants in modern industry. In terms of lanthanide series, the valence configuration shares the typical state of $4f^x5d^{0-1}6s^2$ (x = 1-14). Despite the lower energy of *5s*/*5p* orbitals compared with *4f* orbitals, the occupancy of dispersive *5s*/*5p* orbitals allows for the outside location, which contributes to the weaking shielding of *4f* electrons.[107-109] Benefiting from the intra-atomic *4f-4f* electron transitions and the weak shielding effect from *5s*/*5p* electrons, the insensitive involvement with surrounding molecules for rare-earth species behaves mostly as the electron modulators.[110-112] Additionally, with the property of *4f*-shell-induced radial shrinkage, rare-earth species exhibit the strong spin-orbit coupling and weak ligand field splitting, thus disclosing the unique magnetic properties.[113]

Based on the unique role of rare-earth species, Rao et al initially discovered the direct mechanism of electrochemical UOR by using $NdNiO_3$ as the catalyst.[114] In the direct mechanism, the typical NiO sample delivers the interconversion Ni^{2+}/Ni^{3+} as the crucial step for oxidation of urea molecule alongside the charge transfer step. However, with the incorporation of Nd^{3+}, the retention of high-valence NiOOH phase without the reduction into $Ni(OH)_2$ is observed, providing the sufficient oxidative capacity at the Ni^{3+} site. Benefiting from the exposure of Ni^{3+} sites in $NdNiO_3$, the enhanced adsorption of OH^- is also favored, thus accounting for the well-retained formation of NiOOH. Afterwards, the formation of $NdNiO_3$-NiO heterointerface was also unveiled as interface-driven promotion of electrochemical UOR.[115] The construction of such type of heterointerface enriches the activate NiOOH phase for better UOR performance, where modulated interface of charge distribution optimizes the balance between the adsorption of urea and desorption of $*CO_2$ with the assistance of strong OH^- adsorption. Intrinsically, the scheme of *d-p-f* gradient orbital coupling framework has been constructed to supply the comprehension over rare-earth-induced system for heterogeneous catalysis.[116-118] Taking octahedral and tetrahedral structure as the prototype, the metal-oxygen interaction allows for the formation of non-bonding t_{1g}/t_{2u} states in octahedral site and t_1 states in tetrahedral sites.[119] With the incorporation of rare-earth into octahedral site, the low covalency is able to further induce the weak t_{1u}/t_{2u} bonding states beyond, which is promising to activate the lattice oxygen as the nucleophilic site for modulating the UOR performance.[120,

View Article Online
DOI: 10.1039/D6SC03404G

121

With the notation about the gradient orbital coupling, Qiang et al reported the construction of La-incorporated 3D ordered macroporous NiO heterostructure (3DOM La_2O_3-NiO) catalyst for electrochemical UOR.[122] As shown in Fig. 14a, La element shares the unique configuration of $4f^0$ after the electron loss of valence $6s^2$ states. The gradient orbital coupling within La–O–Ni site can be constructed based on the covalency for Ni–O with bonding and antibonding (Ni–O)* bands, where the σ and π conjunction is contributed by O-*sp* orbitals. Once upon the construction of La–O–Ni gradient orbital coupling framework, the charge transfer between La_2O_3 and NiO can be facilitated with the thermo-balance through the Fermi level leverage, which can be derived from the work function of La_2O_3 (2.70 eV) versus NiO (3.84 eV). The morphology of La_2O_3-NiO in Fig. 14b reveals the even uniformity of good size and abundant porosity with pore wall, providing the favorable mass transport condition during heterogeneous catalysis. To further understand the electronic interaction between La_2O_3 and NiO, the charge density difference in Fig. 14c presents the observable electron transfer from La to Ni through La–O–Ni bridge. For 3DOM La_2O_3-NiO, the well-behaved electrochemical performance reveals the voltages of 1.24 V, 1.30 V, and 1.38 V to approach the current density of 10 mA cm^{-2}, 50 mA cm^{-2}, and 100 mA cm^{-2} respectively. Benefiting from the advantageous performance of 3DOM La_2O_3-NiO, the practical measurement in the membrane electrode assembly (MEA)-based anion exchange membrane water splitting (AEMWE) device with the electrolyte of 1 M KOH + 0.33 M urea solution (Fig. 14d). The proposed reaction mechanism on La–O–Ni bridge is termed as the high valence nickel mechanism (HNM) (Fig. 14e). To be specific, the electrochemical UOR process proceeds through the adsorption of urea onto the Ni site, which is followed by the gradual cleavage of N–H bonds, thus favoring the formation of *OCNN intermediate. It is determined that the PDS of UOR is assigned to be the cleavage of N–H bond of $*OCNH_2NH$ into $*OCNH_2N$ with the free energy gap of 1.22 eV, which is larger than La_2O_3-NiO of 1.04 for the PDS of $*OCNH_2N \rightarrow *OCNHN$ (Fig. 14f). Additionally, Zheng et al also demonstrated the Ce-doped Ni_3S_2 catalyst loaded onto the Ni foam for highly effective UOR.[123] With the construction of gradient orbital coupling of Ce *4f*-S *3p*-Ni *3d*, the d-band center of Ni site is downshifted from -2.46 eV to -3.03 eV, thus weakening the adsorption of

*CO during UOR. With the Ce doping, the corresponding energy barrier for the dehydrogenation of urea is assigned to be 0.22 eV, which is significantly lower than the oxidation of *CO as the RDS (1.68 eV) for the counterpart. Similarly, Zhang et al also reported the Ce-induced NiS catalyst (Ce-NiS) for highly-effective UOR.[124] By tuning the Ce loading content, the performance follows the trend of 3% Ce-NiS > 5% Ce-NiS > 1% Ce-NiS, in which the best-behaved Ce-NiS presents the high Faradaic efficiency of 91.39% compared with NiS of 67.52% for hydrogen production. Furthermore, the electrochemical activation energy of UOR delivers the decreased result of 8.72 kJ/mol to 5.68 kJ/mol with the Ce doping, also confirming the promotive role of Ce.

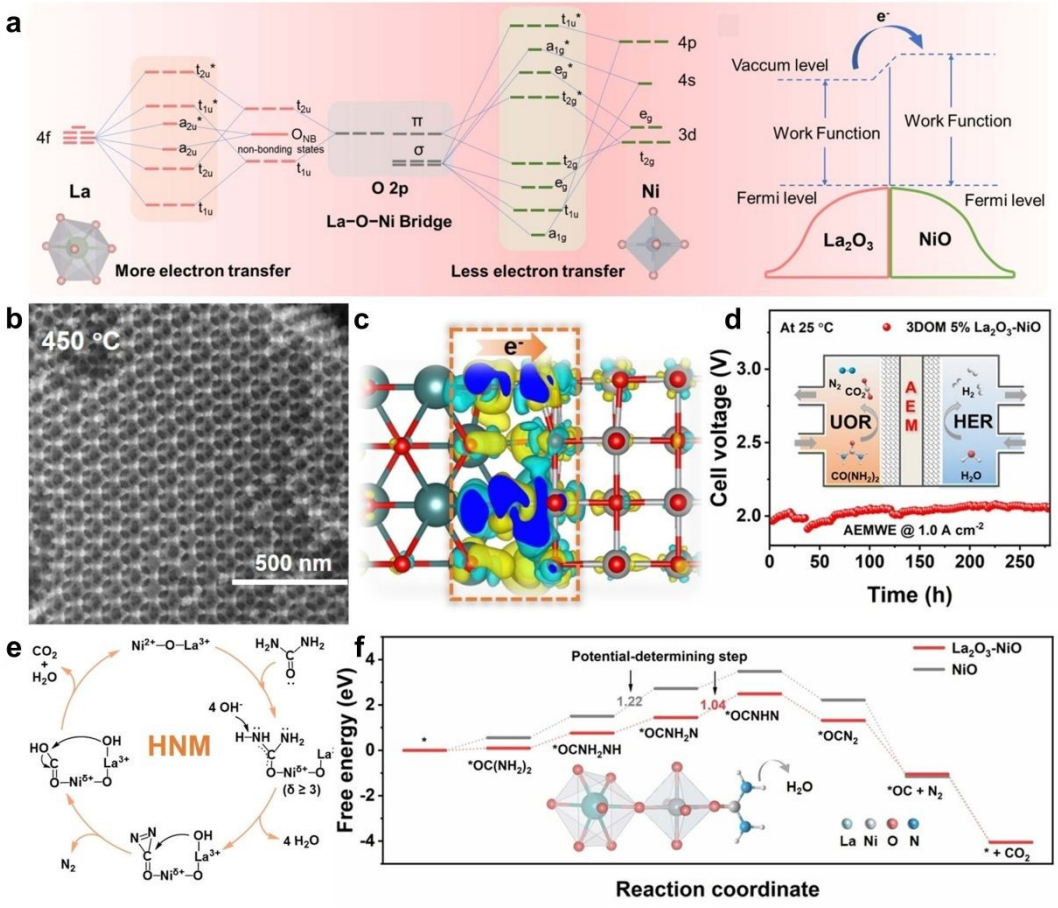

Fig. 14. (a) Qualitative molecular orbital diagram of gradient orbital coupling within the La_2O_3-NiO system; (b) SEM image of La_2O_3-NiO under the calcination temperature of 450 ℃; (c) Charge density difference of La_2O_3-NiO, where the yellow and cyan areas represent the electron accumulation and depletion; (d) Electrochemical stability of UOR coupled with HER at current density of 1 A cm^{-2}; (e) Proposed UOR mechanism over La^{3+}–O–$Ni^{\delta+}$($\delta \geq 3$); (f) Gibbs free energy profile under standard condition of UOR process for La_2O_3-NiO and NiO surfaces.[122]

By noting about the unique role of asymmetric Ce–O–Ni sites, Liu et al reported the self-supported construction of Ce-doped Ni-MOF catalyst (Ce–Ni–BDC) with the assistance of Benzene-1,4-dicarboxylic acid as the ligand (Fig. 15a).[125] Under the solvothermal growth of Ni–BDC over Ni foam, the prepared nanosheets provides the fluffy and biscuit-like structure with abundant interlayers of ~25 nm that favors the ion exchange of Ce^{3+} into Ni-BDC (Fig. 15b). The atomic coordination of Ce–Ni–BDC states the extended Ni–O bond length compared with Ni–BDC, which can be attributed to the formation of Ce–O–Ni site, as shown in Fig. 15c. Accordingly, the Ce–O bond length shows the subtle extension compared with CeO_2 at ~ 1.87 Å, owing to the weaker bond strength with the formation of Ce–O–Ni site (Fig. 15d). The electrochemical performance (Fig. 15e) undergoes the remarkable negative shift of potential of 268 mV in 1 M KOH + 0.5 M urea than in 1 M KOH electrolyte, Ce–Ni–BDC exhibits only 1.261 V at 10 mA cm^{-2} and a Tafel slope of 44.33 mV dec^{-1}, while Ni-BDC presents a higher potential of 1.345 V at 10 mA cm^{-2} and a larger Tafel slope of 73.32 mV dec^{-1}, illustrating the enhancement of UOR activity through the formation asymmetric Ce–O–Ni site. By examining the *in situ* Raman spectroscopy, the distinctive peak of symmetric C–N stretching vibration mode at 1009 cm^{-1} confirms the stable adsorption and transport of urea molecule from 1.2 to 1.7 V (Fig. 15f). Concerning the oxidative environment, the newly formed peaks at 460 and 578 cm-1 can be attributed to Ce-*γ*-NiOOH at potentials over 1.3 V, accompanied by the disappearance of Ce–O–Ni signals. For the Ni–BDC sample, the emergence of peaks at 460 and 563 cm^{-1} stems from γ-NiOOH at potential of 1.45 V, denoting the slower reconstruction process and higher required potential. With the formation of active Ce-γ-NiOOH phase, the Ce site promotes the obvious charge transfer towards Ni sites, which is able to enhance the UOR performance (Fig. 15g). To be specific, the electron transfer from Ce favors the formation of asymmetric Ce–O–Ni within Ce-*γ*-NiOOH, which is consistent with the spectra result, as indicated by Fig. 15h. With the further incorporation of Ce-Ni-BDC catalyst into direct Zn-urea battery as similar to Zn-air battery, the anode reaction proceeds through the electrochemical urea splitting into CO_2 and N_2 in replace of OER (Fig. 15i). Under the periodic shift of current densities, the Galvanostatic discharge-charge profile presents the flexible respondence,

denoting the promisingly practical application (Fig. 15j). Similarly, Wang et al unveiled the industrial-level UOR performance by supplying Ce-doped Ni_5P_4 (Ce-Ni_5P_4) as the catalyst.[126] The introduction of Ce into Ni_5P_4 facilitates the electron transfer from P and Ni towards Ce site, in which the increased chemical state of Ni site boosts the reconstruction into NiOOH with higher UOR kinetics, thus decreasing the energy gap of RDS, deprotonation of *CONHN into *CONN. Besides the use of Ce, the incorporation of La into β-$Ni(OH)_2$ as La:β-$Ni(OH)_2$ also exhibits the fast reaction kinetics, where the electronic interaction between La and Ni ions is delivered to accelerate the electron transport for electrical conductivity, thus adjusting the electrochemical UOR performance.[127]

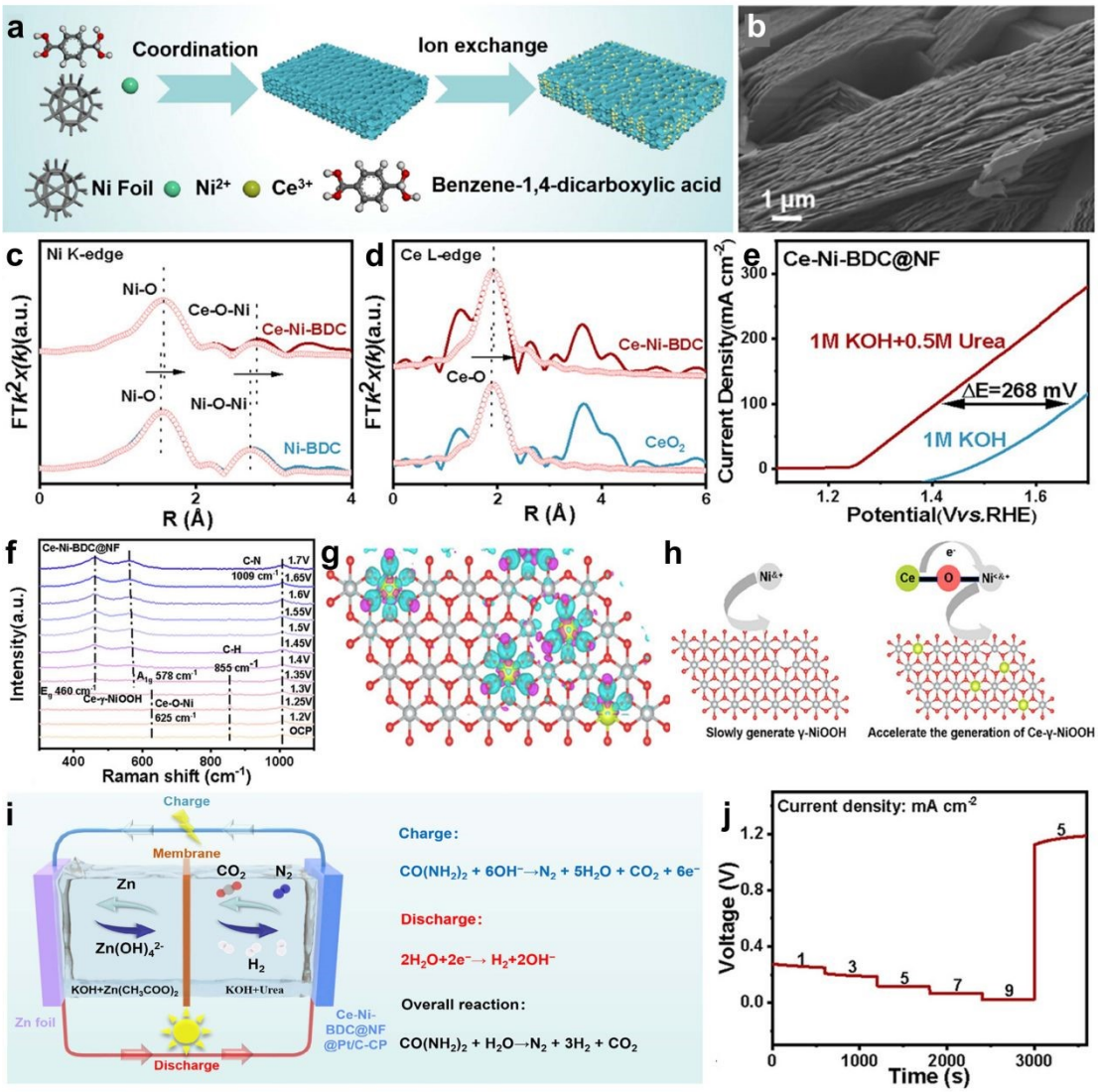

Fig. 15. (a) Schematic synthesis for the Ce–Ni–BDC loaded on Ni foam; (b) SEM image of Ni–BDC; (c) Ni K-edge spectra of Ce–Ni–BDC and Ni–BDC; (d) Ce L-edge spectra for Ce–Ni–BDC with reference to standard CeO_2; (e) Polarization curves of Ce–Ni–BDC for UOR and

View Article Online
DOI: 10.1039/D6SC03404G

OER; (f) Potential-dependent in situ Raman spectra for Ce–Ni–BDC during UOR; (g) Charge density difference for Ce-γ-NiOOH, where cyan and purple regions represent the electron accumulation and depletion respectively; (h) Proposed electron transfer over Ce–Ni–BDC; (i) Schematic diagram of Zn-urea battery; (j) Galvanostatic discharge/charge curves under various current densities.[125] Copyright 2025, Wiley-VCH GmbH.

4. Summary and outlook

In this review, the local hetero-ion modulation over Ni-based catalysts has been systematically focused for electrochemical UOR, where the hetero-ion species range from main group, transition-metal block, towards rare-earth block. Beginning with the discussion of various pathways over Ni-based catalysts, the progress of urea splitting into CO_2 and N_2 can be triggered with the assistance of molecular N–N coupling, nucleophilic attack by O species, and adsorbate evolution. From these distinctive pathways, it can be witnessed that the dynamic phase transformation of Ni-based catalysts shares the vital role from the chemical redox behavior among oxidative $Ni^{\delta+}$ species. To lead the intrinsic comprehension over the complex UOR system, the universal scaling relationships have been constructed based on various energy descriptors. The intrinsic insight over electronic structure modulation by hetero-ion species over various Ni catalyst are exclusively pronounced to supply the structure-performance relation when designing highly-effective Ni-based catalysts. Undoubtedly, these inspiring progresses pave the way for future development in electrochemical urea splitting in replace of highly energy-consuming OER and in the agricultural pollution treatment. To guide the future research and echo for the advancement of data-driven catalysis, a novel outlook is supplied based on closed-loop framework for designing and screening of promising catalysts for UOR (Fig. 16). Notably, although hetero-ion modulation provides an effective regulatory strategy for electrochemical urea oxidation, UOR still faces stability issues. Especially, during the long-term stability test, hetero-ion modulation exhibits no relatively pronounced improvement since it is prone to agglomeration and reconstruction, which severely affects the stability of Ni-based catalysts. Therefore, it is still needed to develop modification design strategies to promote the stability of Ni-based catalysts in electrochemical urea oxidation.

4.1. Data-driven science and theoretical investigation

View Article Online
DOI: 10.1039/D6SC03404G

With the exploit of the abundant data resources reported, the characteristic samples for UOR can be obtained for data compact as the reference source. By concentration on these resources, the key features of experimental data can be further reorganized according to the vectorized properties by large language models (LLMs) to construct the frontier database. During the input of LLMs, the natural language orders take the effect combined with the user plate and typical derivation strategies from artificial intelligence, noted as the prompt engineering (e.g. zero-shot, one-shot, few-shot, chain-of-thought). Afterwards, the theoretical screening for catalysis can be well extended based on these vectorized training dataset with the assistance of machine learning (ML), including the coordination number around Ni (CN_{Ni}), the electronegativity of dopants (χ_d) with contents, mean-field adsorption energy of Ni surface (E_m), coverage of adsorbates (θ), and so forth, constructing the ML-driven relation like $E_m \leftarrow \alpha CN_{Ni} + \beta\chi_d + \gamma\Sigma_i\theta_i$. To reach out for the high accuracy, the first-principle framework should be proceeded over the critical catalytic descriptors for UOR. Thus, with the input of first-principle data resources, the training for machine learning potential (MLP) further provides the radical dismantlement for the dimension and time series limitations of first-principle framework.

4.2. Catalyst synthesis and practical application

With the guidance of data science, the catalyst synthesis can be purposeful by referring to the general properties of target materials for UOR. For instance, the catalyst synthesis can be realized using tailored preparation strategies, such as solid-state reaction, solvothermal reaction, molecular assembly reaction, and atomic layer reaction under corresponding reaction conditions, which aims at the intrinsic synergism between Ni and other active metal sites. After the catalyst synthesis, the instant electrochemical measurement of UOR can be accessed through the multi-functional electrochemical lab, in terms of polarized curves, Tafel slopes, electrochemical impedance, and so forth. Based on the screened catalysts, the practical application can be achieved in comparison of the energy consumption related with OER for validation. Generally, the electrochemical screening for the performance supplies the experimental validation and the materials resources for the physical characterizations, which is also the necessary feedback for the theoretical guidance. Besides, since the metal site typically acts as the main active site, the electrochemical screening of the metal dissolution should be also performed to monitor the catalyst stability for highly-performed UOR performance.

View Article Online
DOI: 10.1039/D6SC03404G

4.3. Advanced physical characterizations

For advanced physical characterizations, catalyst samples are collected both before and after UOR for subsequent physical characterizations to investigate the phase and surface transformation. To be specific, the combination of X-ray-derived spectra and surface information detection provides the pre-catalyst view for the basic properties of the obtained catalyst samples. Concerning the dynamic surface changes during UOR progress, the utilization of operando techniques supply the instant signals of surface coverage of adsorbates and phase composition with the shifting of bias potentials. For urea oxidation, the conversion into N_2 and CO_2 induces the complex surface state change to influence the catalytic behavior for the transformation of adsorbed N_xH_y species. With the capture of these subtle signals, the theoretical modelling can be promisingly rationalized to lead the consistence between time and spatial dimensions for electrochemical urea splinting. In terms of the subtle signal from the metal coordination, its potential-dependent shift should be also determined to analyze the metal dissolution beyond the adsorption and desorption of chemical intermediates during UOR.

Notably, the establishment of the closed-loop framework can significantly accelerate the discovery of highly-performed UOR catalysts and sharpen the microscale comprehension of reaction mechanisms, enabling more efficient exploration of structure-activity relationships and dynamic catalytic processes.

View Article Online
DOI: 10.1039/D6SC03404G

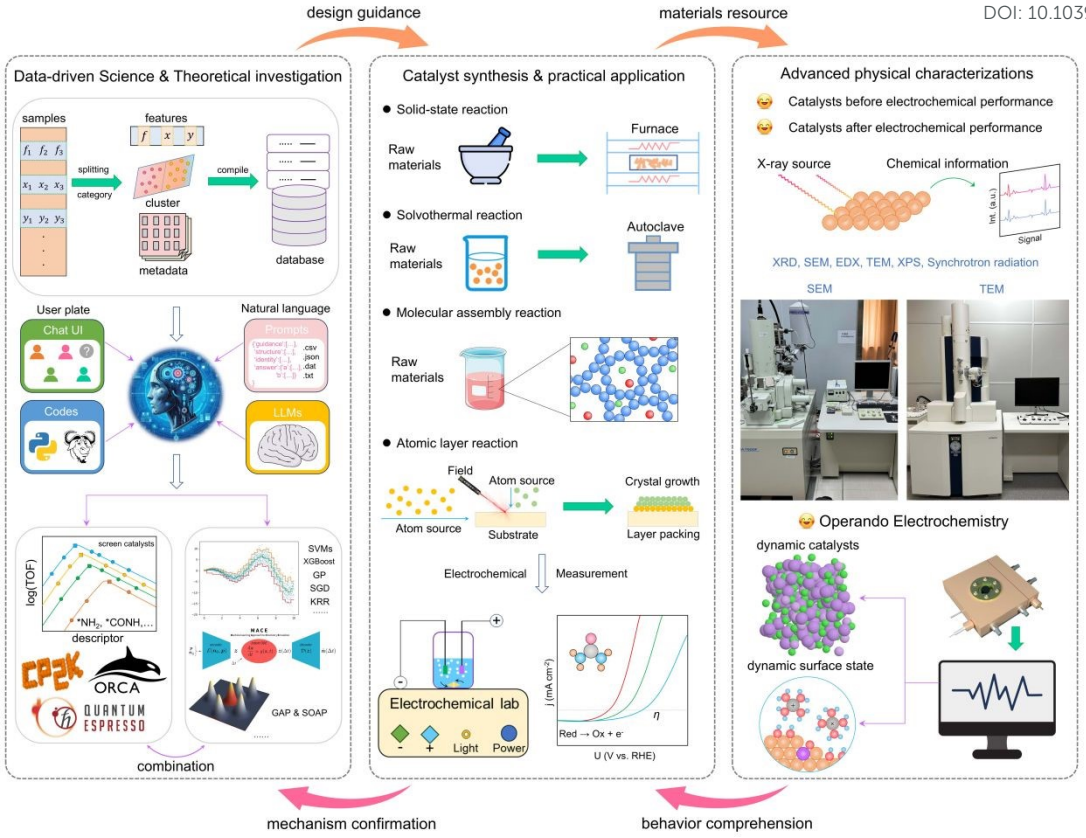

Fig. 16. Closed-loop framework for future investigation of UOR: data-driven science, theoretical investigation, catalyst synthesis and application, and advanced physical characterizations.

Conflicts of interest

The authors declare no competing interests.

Data availability

Data will be made available on request.

Acknowledgements

This work was financially supported by National Natural Science Foundation of China (22279062), Basic Research Program of Jiangsu (BK20250033), 78th General Funding Program of the China Postdoctoral Science Foundation (211090B62508) and JSPS KAKENHI (JP25K01737). The authors are grateful for the supports from National and Local Joint Engineering Research Center of Biomedical Functional Materials and Priority Academic Program Development of Jiangsu Higher Education Institutions. T. Lu acknowledge the Center

View Article Online
DOI: 10.1039/D6SC03404G

for Computational Materials Science, Institute for Materials Research, Tohoku University, for the use of MASAMUNE-IMR (Nos. 202512-SCKXX-0208) and the Institute for Solid State Physics (ISSP) at the University of Tokyo for the computational resources.

References

1. S. Rekker, G. Chen, R. Heede, M. C. Ives, B. Wade and C. Greig, *Nat. Clim. Change*, 2023, **13**, 927-934.
2. R. Wang, W. He, Y. Xue, Y. Yu and B. Liu, *Nat. Food*, 2026, **7**, 27-37.
3. T. J. Wallington, M. Woody, G. M. Lewis, G. A. Keoleian, E. J. Adler, J. R. R. A. Martins and M. D. Collette, *Joule*, 2024, **8**, 2190-2207.
4. H. Lin, Z. Sui, F. Li and W. Wu, *Matter*, 2025, **8**, 102293.
5. Y. Yang, Y. Cheng, J. P. H. Poon, Y. Zhou, X. Qian, S. Xia, X. Li, J. Xue, L. Zhang and H. Zhang, *Nat. Sustain.*, 2025, **8**, 1223-1233.
6. H. Zhang, Y. Zuo and J. Huang, *Chem. Synth.*, 2025, **5**, 52.
7. J. Xu, G. Zhang, S. Fang, J. Li, X. Xiao, Y. Ye, Z. Zhang, R. Xu, J. Zhou, Y. Wu, W. Huang and Y. Cui, *Nat. Chem. Eng.*, 2026, DOI: 10.1038/s44286-026-00362-7.
8. K. R. Bassett, S. F. Hupperts, S. Jämtgård, L. Östlund, J. Fridman, S. S. Perakis and M. J. Gundale, *Nature*, 2026, **650**, 629-635.
9. Y. Zhang, *Nat. Rev. Chem.*, 2017, **1**, 0057.
10. W. Feng, B. Chang, Y. Ren, D. Kong, H. B. Tao, L. Zhi, M. A. Khan, R. Aleisa, M. Rueping and H. Zhang, *Adv. Mater.*, 2025, **37**, 2416012.
11. M. Liu, W. Zou, S. Qiu, N. Su, J. Cong and L. Hou, *Adv. Funct. Mater.*, 2024, **34**, 2310155.
12. G. Zhan, L. Hu, H. Li, J. Dai, L. Zhao, Q. Zheng, X. Zou, Y. Shi, J. Wang, W. Hou, Y. Yao and L. Zhang, *Nat. Commun.*, 2024, **15**, 5918.
13. L. Miao, W. Jia, X. Cao and L. Jiao, *Chem. Soc. Rev.*, 2024, **53**, 2771-2807.
14. Z. Li, L. Sun, Y. Zhang, Y. Han, W. Zhuang, L. Tian and W. Tan, *Coord. Chem. Rev.*, 2024, **510**, 215837.
15. K. Dashtian, S. Shahsavarifar, M. Usman, Y. Joseph, M. R. Ganjali, Z. Yin and M. Rahimi-Nasrabadi, *Coord. Chem. Rev.*, 2024, **504**, 215644.
16. N. Du, C. Roy, R. Peach, M. Turnbull, S. Thiele and C. Bock, *Chem. Rev.*, 2022, **122**, 11830-11895.
17. Y. Gao, H. Yu, W. Wang, P. Chi, S. Liu, H. Rao, C. Bian and J. Ge, *Joule*, 2026, DOI: 10.1016/j.joule.2026.102337.
18. C. R. Wang, J. M. Stansberry, R. Mukundan, H.-M. J. Chang, D. Kulkarni, A. M. Park, A. B. Plymill, N. M. Firas, C. P. Liu, J. T. Lang, J. K. Lee, N. E. Tolouei, Y. Morimoto, C. H. Wang, G. Zhu, J. Brouwer, P. Atanassov, C. B. Capuano, C. Mittelsteadt, X. Peng and I. V. Zenyuk, *Chem. Rev.*, 2025, **125**, 1257-1302.
19. C. Rong, K. Dastafkan, Y. Wang and C. Zhao, *Adv. Mater.*, 2023, **35**, 2211884.
20. Z. Chen, Q. Fan, J. Zhou, X. Wang, M. Huang, H. Jiang and H. Cölfen, *Angew. Chem., Int. Ed.*, 2023, **62**, e202309293.
21. H. Li, Y. Lin, J. Duan, Q. Wen, Y. Liu and T. Zhai, *Chem. Soc. Rev.*, 2024, **53**, 10709-10740.

View Article Online
DOI: 10.1039/D6SC03404G

22. F. Wang and S. S. Stahl, *Acc. Chem. Res.*, 2020, **53**, 561-574.
23. C. Liu, F. Chen, B.-H. Zhao, Y. Wu and B. Zhang, *Nat. Rev. Chem.*, 2024, **8**, 277-293.
24. H. Sun, X. Xu, L. Fei, W. Zhou and Z. Shao, *Adv. Energy Mater.*, 2024, **14**, 2401242.
25. Q. Zhu, J. Xiao, C. Deng, T. Huang, H. Ding, L. Zhang and G. Xu, *Chin. J. Struct. Chem.*, 2025, **44**, 100651.
26. N. Zhao, N. Zhang, K. Liu, S. Liu, Y. Wang, R. Jia, Y. Dai, M. Xue and G. Zhao, *Nano Res. Energy*, 2025, **4**, e9120206.
27. Q. Li, J. Wang, Y. Shi, H. Li, H. Yang, K. Xiang, W. You and J. Liang, *Mater. Horiz.*, 2025, **12**, 9952-9965.
28. X. Gao, S. Zhang, P. Wang, M. Jaroniec, Y. Zheng and S.-Z. Qiao, *Chem. Soc. Rev.*, 2024, **53**, 1552-1591.
29. X. Wang, J.-P. Li, Y. Duan, J. Li, H. Wang, X. Yang and M. Gong, *ChemCatChem*, 2022, **14**, e202101906.
30. P. Qiao, G. Li, X. Xu, D. Wang, F. Wang, L. Xu, L. Lu, H. Cong and M. Sun, *Adv. Funct. Mater.*, 2025, **35**, 2421136.
31. S. Xu, X. Ruan, M. Ganesan, J. Wu, S. K. Ravi and X. Cui, *Adv. Funct. Mater.*, 2024, **34**, 2313309.
32. H. Jiang, M. Sun, S. Wu, B. Huang, C.-S. Lee and W. Zhang, *Adv. Funct. Mater.*, 2021, **31**, 2104951.
33. R. K. Singh, K. Rajavelu, M. Montag and A. Schechter, *Energy Technol.* , 2021, **9**, 2100017.
34. J. Gautam, S.-Y. Lee and S.-J. Park, *Adv. Energy Mater.*, 2025, **15**, 2406047.
35. J. Li, S. Wang, J. Chang and L. Feng, *Adv. Powder Mater.*, 2022, **1**, 100030.
36. W. Liu, X. Niu, J. Tang, Q. Liu, J. Luo, X. Liu and Y. Zhou, *Chem. Synth.*, 2023, **3**, 44.
37. G. Gnana kumar, A. Farithkhan and A. Manthiram, *Adv. Energy Sustainability Res.*, 2020, **1**, 2000015.
38. C. Zhang, S. Chen, L. Guo, Z. Li, C. Yan and C. Lv, *Chin. J. Chem.*, 2024, **42**, 3441-3468.
39. Q.-X. Huang, F. Wang, Y. Liu, B.-Y. Zhang, F.-Y. Guo, Z.-Q. Jia, H. Wang, T.-X. Yang, H.-T. Wu, F.-Z. Ren and T.-F. Yi, *Rare Met.*, 2024, **43**, 3607-3633.
40. X. Tang, Y. Xin, R. Chen, X. Ren, L. Gao, H. Xu, P. Yang and A. Liu, *J. Mater. Chem. A*, 2025, **13**, 34122-34148.
41. S. Lu, X. Zheng, L. Fang, F. Yin and H. Liu, *Electrochem. Commun.*, 2023, **157**, 107599.
42. A. S. Rasal, H. M. Chen and W.-Y. Yu, *Nano Energy*, 2024, **121**, 109183.
43. Q. Qian, Y. Zhu, N. Ahmad, Y. Feng, H. Zhang, M. Cheng, H. Liu, C. Xiao, G. Zhang and Y. Xie, *Adv. Mater.*, 2024, **36**, 2306108.
44. W. Li, X. Lu and Z. Li, *Adv. Energy Mater.*, 2026, **16**, e04716.
45. Q. Li, Y. Wang, T. Pan, Y. Zhu and H. Pang, *Sci. China Mater.*, 2025, **68**, 317-340.
46. K. Dashtian, S. Shahsavarifar, M. Usman, Y. Joseph, M. R. Ganjali, Z. Yin and M. Rahimi-Nasrabadi, *Coord. Chem. Rev.*, 2024, **504**, 215644.
47. J. Wang, M. Sun, X. Zhang, J. Liu, J. He, W. Ge, S. Kong, G. Zhang, M. Gao, Z. Sun and X. Shi, *Adv. Mater.*, 2026, **38**, e15043.
48. T. Li, Z. Zheng, Z. Chen, M. Zhang, Z. Liu, H. Chen, X. Xiao, S. Wang, H. Qu, Q. Fu, L. Liu, M. Zhou, B. Wang and G. Zhou, *Energy Environ. Sci.*, 2025, **18**, 4996-5008.

49. J. Liang, S. Zhu, D. Chen, Y. Li, D. Zhou, N. Meng, Y. Liao, H. Sun and J. Kong, *Adv. Powder Mater.*, 2025, **4**, 100344.
50. Q. Jin, M. X. Garcia-Ortiz and L. Árnadóttir, *J. Catal.*, 2026, **453**, 116503.
51. C.-J. Huang, H.-M. Xu, T.-Y. Shuai, Q.-N. Zhan, Z.-J. Zhang and G.-R. Li, *Small*, 2023, **19**, 2301130.
52. B. Zhu, Z. Liang and R. Zou, *Small*, 2020, **16**, 1906133.
53. J. Wang, Y. Sun, Y. Qi and C. Wang, *ACS Appl. Mater. Interfaces*, 2021, **13**, 57392-57402.
54. Z. Ma, X. Liu, H. Wang, L. Xie, Z. Sun, H. Zhan, X. Mi, S. Zhan and Q. Zhou, *Adv. Energy Mater.*, 2026, **16**, e02563.
55. H. Zhang, X. Meng, J. Zhang and Y. Huang, *ACS Sustainable Chem. Eng.*, 2021, **9**, 12584-12590.
56. M. Song, X. Yang, C. Guo, S. Zhang, J. Ma and H. Gao, *EcoEnergy*, 2025, **3**, 470-481.
57. S. Ding, J. Duan and S. Chen, *EcoEnergy*, 2024, **2**, 45-82.
58. T. D. Kühne, M. Iannuzzi, M. Del Ben, V. V. Rybkin, P. Seewald, F. Stein, T. Laino, R. Z. Khaliullin, O. Schütt, F. Schiffmann, D. Golze, J. Wilhelm, S. Chulkov, M. H. Bani-Hashemian, V. Weber, U. Borštnik, M. Taillefumier, A. S. Jakobovits, A. Lazzaro, H. Pabst, T. Müller, R. Schade, M. Guidon, S. Andermatt, N. Holmberg, G. K. Schenter, A. Hehn, A. Bussy, F. Belleflamme, G. Tabacchi, A. Glöß, M. Lass, I. Bethune, C. J. Mundy, C. Plessl, M. Watkins, J. VandeVondele, M. Krack and J. Hutter, *J. Chem. Phys.*, 2020, **152**, 194103.
59. J. VandeVondele, M. Krack, F. Mohamed, M. Parrinello, T. Chassaing and J. Hutter, *Comput. Phys. Commun.*, 2005, **167**, 103-128.
60. J. VandeVondele and J. Hutter, *J. Chem. Phys.*, 2007, **127**, 114105.
61. M. Krack, *Theor. Chem. Acc.*, 2005, **114**, 145-152.
62. J. Hutter, M. Iannuzzi, F. Schiffmann and J. VandeVondele, *Wiley Interdiscip. Rev.:Comput. Mol. Sci.*, 2014, **4**, 15-25.
63. C. Hartwigsen, S. Goedecker and J. Hutter, *Phys. Rev. B*, 1998, **58**, 3641-3662.
64. S. Grimme, S. Ehrlich and L. Goerigk, *J. Comput. Chem.*, 2011, **32**, 1456-1465.
65. S. Grimme, J. Antony, S. Ehrlich and H. Krieg, *J. Chem. Phys.*, 2010, **132**, 154104.
66. S. Goedecker, M. Teter and J. Hutter, *Phys. Rev. B*, 1996, **54**, 1703-1710.
67. S. Grimme, *Chem. - Eur. J.*, 2012, **18**, 9955-9964.
68. J. Zhang, J. Zhu, L. Kang, Q. Zhang, L. Liu, F. Guo, K. Li, J. Feng, L. Xia, L. Lv, W. Zong, P. R. Shearing, D. J. L. Brett, I. P. Parkin, X. Song, L. Mai and G. He, *Energy Environ. Sci.*, 2023, **16**, 6015-6025.
69. J. Li, C. Yin, S. Wang, B. Zhang and L. Feng, *Chem. Sci.*, 2024, **15**, 13659-13667.
70. Y. Luo, H. Zhou and Y. Tong, *ChemSusChem*, 2026, **19**, e202502504.
71. J. Jian, Y. Qiao, F. Chen, C. Liu, W. Liu, Z. Li, M. Pi, Z. Li and Z. Zou, *Appl. Catal., B*, 2025, **374**, 125390.
72. B. K. Boggs, R. L. King and G. G. Botte, *Chem. Commun.*, 2009, DOI: 10.1039/B905974A, 4859-4861.
73. D. A. Daramola, D. Singh and G. G. Botte, *J. Mater. Chem. A*, 2010, **114**, 11513-11521.
74. J. Li, J. Li, T. Liu, L. Chen, Y. Li, H. Wang, X. Chen, M. Gong, Z.-P. Liu and X. Yang, *Angew. Chem., Int. Ed.*, 2021, **60**, 26656-26662.

75. W. Chen, L. Xu, X. Zhu, Y.-C. Huang, W. Zhou, D. Wang, Y. Zhou, S. Du, Q. Li, C. Xie, L. Tao, C.-L. Dong, J. Liu, Y. Wang, R. Chen, H. Su, C. Chen, Y. Zou, Y. Li, Q. Liu and S. Wang, *Angew. Chem., Int. Ed.*, 2021, **60**, 7297-7307.
76. L. F. Huang, M. J. Hutchison, R. J. Santucci, Jr., J. R. Scully and J. M. Rondinelli, *J. Phys. Chem. C*, 2017, **121**, 9782-9789.
77. W. Sun, N. Govindarajan, A. Prajapati, J. Huang, H. Bemana, J. T. Feaster, S. A. Akhade, N. Kornienko and C. Hahn, *ACS Appl. Mater. Interfaces*, 2025, **17**, 2365-2375.
78. Y. Zhou and N. López, *ACS Catal.*, 2020, **10**, 6254-6261.
79. B. Hammer and J. K. Norskov, *Nature*, 1995, **376**, 238-240.
80. M. T. Greiner, T. E. Jones, S. Beeg, L. Zwiener, M. Scherzer, F. Girgsdies, S. Piccinin, M. Armbrüster, A. Knop-Gericke and R. Schlögl, *Nat. Chem.*, 2018, **10**, 1008-1015.
81. F. Abild-Pedersen, J. Greeley, F. Studt, J. Rossmeisl, T. R. Munter, P. G. Moses, E. Skúlason, T. Bligaard and J. K. Nørskov, *Phys. Rev. Lett.*, 2007, **99**, 016105.
82. V. Ivanistsev, R. Cepitis, J. Rossmeisl and N. Kongi, *Chem. Soc. Rev.*, 2025, **54**, 10956-10976.
83. K. Chan and J. K. Nørskov, *J. Phys. Chem. Lett.*, 2015, **6**, 2663-2668.
84. S. Ringe, C. G. Morales-Guio, L. D. Chen, M. Fields, T. F. Jaramillo, C. Hahn and K. Chan, *Nat. Commun.*, 2020, **11**, 33.
85. X. Zheng, Y. Mei, Y. Zeng, Q. Hua and S. Lu, *Ind. Chem. Mater.*, 2026, DOI: 10.1039/D5IM00252D.
86. X.-F. Cheng, L.-H. Jiang, X.-P. Zhao, W. Ye, S.-X. Wei, J.-H. He and Z.-B. Zhan, *ACS Appl. Mater. Interfaces*, 2025, **17**, 26766-26774.
87. A. J. Tkalych, K. Yu and E. A. Carter, *J. Phys. Chem. C*, 2015, **119**, 24315-24322.
88. X. Zhu, X. Dou, J. Dai, X. An, Y. Guo, L. Zhang, S. Tao, J. Zhao, W. Chu, X. C. Zeng, C. Wu and Y. Xie, *Angew. Chem. Int. Ed.*, 2016, **55**, 12465-12469.
89. Y. Tong, P. Chen, M. Zhang, T. Zhou, L. Zhang, W. Chu, C. Wu and Y. Xie, *ACS Catal.*, 2018, **8**, 1-7.
90. Z. Ji, Y. Song, S. Zhao, Y. Li, J. Liu and W. Hu, *ACS Catal.*, 2022, **12**, 569-579.
91. Z. Zhao, T. Kang, Y. Dong, Y. Zhou, M. Yuan, H. Xu, J. Wang, G. Qiu, J. Ye and X. Chang, *Appl. Catal. B: Environ. Energy*, 2026, **386**, 126405.
92. S.-K. Geng, Y. Zheng, S.-Q. Li, H. Su, X. Zhao, J. Hu, H.-B. Shu, M. Jaroniec, P. Chen, Q.-H. Liu and S.-Z. Qiao, *Nat. Energy*, 2021, **6**, 904-912.
93. Z. Zhao, H. Zeng, Y. Zhou, M. Yuan and X. Chang, *Appl. Catal., B*, 2025, **375**, 125414.
94. G. Assat and J.-M. Tarascon, *Nat. Energy*, 2018, **3**, 373-386.
95. M. Ben Yahia, J. Vergnet, M. Saubanère and M.-L. Doublet, *Nat. Mater.*, 2019, **18**, 496-502.
96. B. Kim, J.-H. Song, D. Eum, S. Yu, K. Oh, M. H. Lee, H.-Y. Jang and K. Kang, *Nat. Sustain.*, 2022, **5**, 708-716.
97. D.-H. Seo, J. Lee, A. Urban, R. Malik, S. Kang and G. Ceder, *Nat. Chem.*, 2016, **8**, 692-697.
98. D. A. Kitchaev, J. Vinckeviciute and A. Van der Ven, *J. Am. Chem. Soc.*, 2021, **143**, 1908-1916.
99. W.-K. Han, J.-X. Wei, K. Xiao, T. Ouyang, X. Peng, S. Zhao and Z.-Q. Liu, *Angew. Chem., Int. Ed.*, 2022, **61**, e202206050.

100. L. Wang, Y. Zhu, Y. Wen, S. Li, C. Cui, F. Ni, Y. Liu, H. Lin, Y. Li, H. Peng and B. Zhang, *Angew. Chem., Int. Ed.*, 2021, **60**, 10577-10582.
101. M. Liu, W. Zou, S. Qiu, N. Su, J. Cong and L. Hou, *Adv. Funct. Mater.*, 2024, **34**, 2310155.
102. W. Jiang, Z. Zhai, J. Wu and S. Yin, *J. Colloid Interface Sci.*, 2026, **702**, 138869.
103. H. Sun, Z. Luo, M. Chen, T. Zhou, B. Wang, B. Xiao, Q. Lu, B. Zi, K. Zhao, X. Zhang, J. Zhao, T. He, J. Zhang, H. Cui, F. Liu, C. Wang, D. Wang and Q. Liu, *ACS Nano*, 2024, **18**, 35654-35670.
104. L. Cai, H. Bai, J. Li, F. Xie, K. Jiang, Y.-R. Lu, H. Pan and Y. Tan, *Energy Environ. Sci.*, 2025, **18**, 2415-2425.
105. C. Xie, C. Zhou, Y. Zhang, B. Zhou, Y. Yao, B. Li, J. Li, J. Bai, M. Long, K. Jiang, H. Zhu and L. Zhang, *Angew. Chem., Int. Ed.,* 2026, **65**, e25119.
106. G. Zhan, L. Hu, H. Li, J. Dai, L. Zhao, Q. Zheng, X. Zou, Y. Shi, J. Wang, W. Hou, Y. Yao and L. Zhang, *Nat. Commun.*, 2024, **15**, 5918.
107. Z. Wang, Y. Wang, J. Wang, Y. Song, M. J. Robson, A. Seong, M. Yang, Z. Zhang, A. Belotti, J. Liu, G. Kim, J. Lim, Z. Shao and F. Ciucci, *Nat. Catal.*, 2022, **5**, 777-787.
108. H. Fu, Y. Jiang, M. Zhang, Z. Zhong, Z. Liang, S. Wang, Y. Du and C. Yan, *Chem. Soc. Rev.*, 2024, **53**, 2211-2247.
109. Y. Jiang, H. Fu, Z. Liang, Q. Zhang and Y. Du, *Chem. Soc. Rev.*, 2024, **53**, 714-763.
110. H. Wang, S. Yang, W. Fan, Y. Cui, G. Gong, L. Jiao, S. Chen and J. Qi, *ACS Appl. Mater. Interfaces*, 2025, **17**, 14749-14772.
111. M. Li, X. Wu, K. Liu, Y. Zhang, X. Jiang, D. Sun, Y. Tang, K. Huang and G. Fu, *J. Energy Chem.*, 2022, **69**, 506-515.
112. Z. Liu, S. Lee, T. Zhou, J. Yang and T. Yu, *J. Colloid Interface Sci.*, 2025, **692**, 137542.
113. S. Zhang, Y. Jiang, J. Zhao and Y. Du, *Chem. Soc. Rev.*, 2026, **55**, 1494-1513.
114. N. N. Rao, C. Alex, M. Mukherjee, S. Roy, A. Tayal, A. Datta and N. S. John, *ACS Catal.*, 2024, **14**, 981-993.
115. N. N. Rao, C. Alex, S. Tomar, M. S. Naduvil Kovilakath, S.-C. Lee, S. Bhattacharjee and N. S. John, *Appl. Catal., B*, 2025, **371**, 125177.
116. X. Wang, J. Wang, P. Wang, L. Li, X. Zhang, D. Sun, Y. Li, Y. Tang, Y. Wang and G. Fu, *Adv. Mater.*, 2022, **34**, 2206540.
117. M. Li, X. Wang, K. Liu, H. Sun, D. Sun, K. Huang, Y. Tang, W. Xing, H. Li and G. Fu, *Adv. Mater.*, 2023, **35**, 2302462.
118. L. Sun, X. Li, J. Li, Y. Zeng and S. Lu, *Energy Fuels*, 2025, **39**, 13969-13996.
119. X. Wang, J. Hu, T. Lu, H. Wang, D. Sun, Y. Tang, H. Li and G. Fu, *Angew. Chem., Int. Ed.*, 2025, **64**, e202415306.
120. P. Jiang, B. Ge, J. Liu, C. Huang and X. F. Lu, *Appl. Catal., B*, 2026, **380**, 125781.
121. S. Ajmal, A. Rasheed, W. Sheng, G. Dastgeer, Q. A. T. Nguyen, P. Wang, P. Chen, S. Liu, V. Q. Bui, M. Zhu, P. Li and D. Wang, *Adv. Mater.*, 2025, **37**, 2412173.
122. X. Qiang, Y. Yao, J. Yin, P. Da, Z. Mu, K. Shen, Y. Sun, Y. Zhang, P. Li, Z. Li, P. Xi and C.-H. Yan, *Angew. Chem., Int. Ed.*, 2025, **64**, e202424014.
123. W. Zheng, N. Duan, Y. Yang, P. Wang, Y. Qu, C. Zong and Q. Chen, *Inorg. Chem.*, 2024, **63**, 14602-14608.
124. Y. Zhang, W. Zhang, J. Huang, W. Cai and Y. Lai, *EES Catal.*, 2024, **2**, 1306-1313.

125. D. Liu, X. Guo, T. Yang, A. Kong, D. Lv, Y. Yang, X. Cui and R. Liu, *Adv. Funct. Mater.*, 2025, **36**, e17562.
126. Y. Wang, L. Liang, Y. Tang, W. Xiao, T. Zhou, P. Shen and P. Tsiakaras, *Chem. Eng. J.* , 2025, **520**, 165516.
127. P. Hao, Y. Xin, Q. Wang, L. Li, Z. Zhao, H. Wen, J. Xie, G. Cui and B. Tang, *Chem. Commun.*, 2021, **57**, 2029-2032.

View Article Online
DOI: 10.1039/D6SC03404G

The authors confirm that the data supporting this review are available on request.